Monthly Notices
of the
ROYAL ASTRONOMICAL SOCIETY

MNRAS **494,** 1095–1113 (2020)
Advance Access publication 2020 March 13

doi:10.1093/mnras/staa676

Isotopologues of dense gas tracers in nearby infrared bright galaxies

Fei Li,[1,2]★ Junzhi Wang,[1,3]★ Min Fang,[4] Shanghuo Li,[1,2,5] Zhi-Yu Zhang,[6] Yu Gao[7,8] and Minzhi Kong[9]★

[1]*Shanghai Astronomical Observatory, Chinese Academy of Sciences, 80 Nandan Road, Shanghai 200030, China*
[2]*University of Chinese Academy of Sciences, 19A Yuquanlu, Beijing 100049, China*
[3]*Key Laboratory of Radio Astronomy, Chinese Academy of Sciences, Nanjing 210008, China*
[4]*Department of Astronomy, University of Arizona, 933 North Cherry Avenue, Tucson, AZ 85721, USA*
[5]*Harvard-Smithsonian Center for Astrophysics, 60 Garden Street, Cambridge, MA 02138, USA*
[6]*School of Astronomy and Space Science, Nanjing University, 163 Xianlin Road, Nanjing 210023, China*
[7]*Department of Astronomy, Xiamen University, Xiamen, Fujian 361005, China*
[8]*Purple Mountain Observatory, Chinese Academy of Sciences, 8 Yuanhua Road, Nanjing 210034, China*
[9]*Hebei Normal University, No. 20 Road East. 2nd Ring South, Yuhua District, Shijiazhuang, Hebei 050024, China*

Accepted 2020 March 5. Received 2020 February 23; in original form 2019 April 1

ABSTRACT

We present 1 and 3 mm observations of the ^{13}C- and ^{15}N-bearing isotopologues of dense gas tracers towards eight nearby infrared-bright galaxies. With the Institut de Radioastronomie Millimétrique 30-m telescope, we observed the $J = 1$–0 transitions of H^{13}CN, HC^{15}N, H^{13}CO$^+$, HN^{13}C, and H^{15}NC towards M 82, NGC 3079, IC 694, Mrk 231, and NGC 6240. The $J = 3$–2 transition of H^{13}CN was obtained in M 82, NGC 3079, NGC 3504, NGC 4418, NGC 6240, and NGC 6946, using the 10-m Submillimeter Telescope (SMT). We report the first detections of HN^{13}C $J = 1$–0 and H^{13}CN $J = 3$–2 in M 82, and H^{13}CN $J = 3$–2 in NGC 6240 and NGC 3079. We find different line profiles between the $J = 1$–0 and 3–2 transitions of H^{13}CN in both M 82 and NGC 3079. The optical depths of HCN show significant variations among the sample, indicating that dense gas masses estimated from the line luminosities of HCN $J = 1$–0 and 3–2 should be treated with caution for individual galaxies. Optical depth of HCN $J = 3$–2 is found to be higher than that of HCN $J = 1$–0 in M 82, NGC 3079, NGC 4418, and NGC 6240, which indicates that ground state transitions of dense gas tracers might better trace the star-forming gas than the high-J transitions. Based on the H^{13}CN/HC^{15}N line ratios, with the double-isotopic method, low ^{14}N/^{15}N abundance ratios of 120 and 140 are found in NGC 3079 and Mrk 231, respectively.

Key words: galaxies: individual: M 82, NGC 3079, NGC 3504, IC 694, NGC 4418, MrK 231, NGC 6946, NGC 6240.

1 INTRODUCTION

Observational evidence suggests that star formation is closely related to dense cores of molecular clouds in the Milky Way and external galaxies (Lada 1992; Kohno, Kawabe & Vila-Vilaró 1999; Kennicutt & Evans 2012). Studies of dense molecular gas in galaxies, including mass, excitation conditions, spatial distribution, and kinematics, are essential for our understanding of the evolution of galaxies (Mo, van den Bosch & White 2010). The dense gas component traced by the s- called dense gas tracers, e.g. multiple transitions of HCN, HCO$^+$, and CS, which have high dipole moments and thus high critical densities[1] ($n_{\rm crit}$(H$_2$) > 10^4 cm^{-3}), represent the molecular content that is directly involved in forming stars (Mauersberger & Henkel 1989; Nguyen et al. 1992; Paglione, Jackson & Ishizuki 1997; Kohno 2005). These dense gas tracers provide an important tool for investigating principles and physics of star formation in galaxies, for instance, the tight linear correlation between the luminosities of HCN $J = 1$–0 and infrared (IR) emission in global galaxies (Gao & Solomon 2004b) and its further extension to star-forming regions in the Milky Way (Wu et al. 2005; Shimajiri et al. 2017).

Despite the large excitation ranges and different chemical abundances in different galaxies (Greve et al. 2009), these dense gas tracers are normally optically thick. Therefore, there is a large uncertainty in estimating the dense gas mass from a single transition line of a high dipole moment molecule, which is similar to the issue of the CO-to-H$_2$ conversion factors (Narayanan et al. 2012; Papadopoulos 2007). With multiple transitions of individual molecular species, Large Velocity Gradient (LVG) modelling can derive the physical properties of molecular gas, especially the volume density

★ E-mail: lifei@shao.ac.cn (FL); jzwang@shao.ac.cn (JW); confucious76@163.com (MK)

[1]All critical densities ($n_{\rm crit}$) in this work are calculated on the assumption of $T_{\rm kin} = 100$ K and optically thin conditions (Tan et al. 2018).

and excitation temperature (Nguyen et al. 1992; Greve et al. 2009; Izumi et al. 2013; Papadopoulos et al. 2014; Gallagher et al. 2018). Observations of HCN $J = 1$–0, 3–2, and 4–3 lines towards nearby galaxies were obtained in several works (Gao & Solomon 2004a; Krips et al. 2008; Papadopoulos et al. 2014; Zhang et al. 2014; Spilker et al. 2014; Saito et al. 2018). However, it is still difficult to accurately characterize the physical conditions of dense molecular gas with only optically thick lines. For example, the gas densities derived from different molecules (e.g. HCN and HCO^+) are found to differ by approximately a factor of 10 in Arp 220 (Greve et al. 2009).

Emission lines of the rare isotopologues of dense gas tracers, benefitted by their small optical depth, are important to help diagnose these dense gas mass and excitation condition issues. Under reasonable assumptions of isotopic abundance ratios (Henkel et al. 1998; Martín et al. 2010) and local thermal equilibrium (LTE) conditions, optical depths of dense gas tracers can be estimated from their line ratios (Wang et al. 2014, 2016). However, the isotopic lines of dense gas tracers are too faint to be detected in most galaxies, resulting in only few detections in nearby galaxies (Henkel et al. 1998; Wang et al. 2014, 2016; Tunnard et al. 2015; Tang et al. 2019).

This paper presents observations of the ^{13}C- and ^{15}N-bearing isotopic species of dense gas tracers with the Institut de Radioastronomie Millimétrique (IRAM) 30-m telescope in the 3-mm band, including $H^{13}CN$, $HC^{15}N$, $H^{13}CO^+$, $HN^{13}C$, and $H^{15}NC$ $J = 1$–0 towards five nearby IR bright galaxies, as well as $H^{13}CN$ $J = 3$–2 with the 10-m Sub-Millimeter Telescope (SMT) in the 1-mm band, towards six nearby IR bright galaxies. We also perform detailed comparison between the $H^{13}CN$ $J = 1$–0 and 3–2 transitions in these galaxies, since these were designed in this way using different telescopes yet having similar telescope beam sizes of these two observations. We describe the observations and data reduction in Section 2. The main results are presented in Section 3. Section 4 contains the analysis and discussion. The final conclusions are summarized in Section 5.

2 OBSERVATIONS AND DATA REDUCTION

We selected a sample of 37 nearby IR bright galaxies from the far-IR survey of the Infrared Astronomical Satellite (IRAS, Sanders et al. 2003). 33 sources of this sample have 60 μm flux densities of $>$ 20 Jy. The remaining four sources were selected because of their strong HCN 1–0 emission as measured by Gao & Solomon (2004a). A detailed discussion about the detections of HCN 3–2 will be part of another paper (Li et al. 2020). In this paper, we present results for the ^{13}C- and ^{15}N-bearing isotopologues of dense gas tracers towards eight nearby IR-bright galaxies.

2.1 Observations with the SMT 10-m telescope

We carried out HCN $J = 3$–2 observations with the 10-m Submillimeter Telescope (SMT) on the Mount Graham, Arizona, USA, between 2015 December and 2016 February. From this sample we select six targets – M 82, NGC 3504, NGC 3079, NGC 4418, NGC 6240, and NGC 6946 – those with strongest HCN $J = 3$–2 emission, to measure with deep integration the isotopologue $H^{13}CN$ in the $J = 3$–2. The beam sizes of the SMT at 265.886 GHz for HCN $J = 3$–2 and 259.012 GHz for $H^{13}CN$ $J = 3$–2 are 28 and 29 arcsec, respectively. We employed the Atacama Large Millimeter/submillimeter Array (ALMA) Band 6 receiver for the observations. This receiver has dual-polarization sideband-separating mixers. We configured the $H^{13}CN$ $J = 3$–2 line to be observed with the lower sideband (LSB). The backend employs a Forbes filter bank system, which has an 1 MHz frequency spacing and 1024 channels for each polarization. The channel width corresponds to a velocity separation of $\sim$1.2 km s^{-1} at the observing frequency. Beam switching mode with a subreflector throw of 2 arcmin was used for all observations. The telescope pointing and focus were calibrated every two hours, using Jupiter and Mars. The typical system temperature was less than 240 K for all observations. The antenna temperature T_A^* was converted to main beam brightness temperature T_{mb} using $T_{mb} = T_A^*/\eta_b$. The main beam efficiency η_b is 0.77. The integration time of HCN $J = 3$–2 was approximately 30 min for each source. 5–11 h of integration time for the $H^{13}CN$ 3–2 line were used for each source. Details of the observations for the six galaxies are summarized in Table A1.

2.2 Observations with the IRAM 30-m telescope

The observations of rare isotopic lines of dense-gas tracers, which include $H^{13}CN$ 1–0, $H^{13}CO^+$ 1–0, $HN^{13}C$ 1–0, $HC^{15}N$ 1–0, and $H^{15}NC$ 1–0, were carried out with the IRAM 30-m millimetre telescope at Pico Veleta, Spain, in 2017 July. M 82, NGC 6240, and NGC 3079, with a previous detection of $H^{13}CN$ 3–2 and two other strong far-IR emission sources (Mrk 231 and IC 694) were selected for observation. The Eight Mixer Receiver (EMIR) with dual-polarization and the Fourier Transform Spectrometers (FTS) backend with 8 GHz frequency coverage and 195 kHz spectral resolution were used in wobbler switching mode, with beam throws of $\pm$60 arcsec and a switching frequency of 0.5 Hz. Pointing was checked every 2 h with nearby strong millimetre emitting quasi-stellar objects. The EMIR receiver can provide two bands simultaneously. In order to verify that the signal is from the sky frequency rather than radio-frequency interference (RFI) at the IF frequency or from the backend, different local oscillator (LO) tuning setups were used during the observations (see Table A2). The beam sizes of the IRAM 30-m telescope are approximately 29 and 16 arcsec at 87 and 145 GHz, respectively. The typical system temperatures are less than 100 K in the 3-mm band and around 120 K in the 2-mm band. Note that the beam size for the 3-mm band of the IRAM 30-m telescope is almost the same as that of the 1-mm band of the SMT 10-m telescope.The antenna temperature (T_A^*) was converted to the main beam brightness temperature (T_{mb}), using $T_{mb} = T_A^* \cdot F_{eff}/B_{eff}$, where the forward efficiency F_{eff} is 0.95 and beam efficiency B_{eff} is 0.81 for 3-mm band. Every 2 min, we read out one spectrum. The total telescope times ranges from 5 to 13 h towards each source.

2.3 Data reduction

We list the basic parameters of our sample of sources in Table 1. The CLASS package, which is a part of the GILDAS[2] software, is used for data reduction. First, we check each spectrum and remove spectra with poor qualities. Then, we average all reliable spectra of a given source into one spectrum. A first-order polynomial baseline was fitted and subtracted from the averaged spectrum for each source. The rest frequencies of the isotopic lines from the NIST data base *Recommended Rest Frequencies for Observed Interstellar Molecular Microwave Transitions*[3] were used for the line identification. The average spectra were smoothed to velocity

[2] http://www.iram.fr/IRAMFR/GILDAS
[3] https://pml.nist.gov/cgi-bin/micro/table5/start.pl

Table 1. Sample of galaxies.[a]

Galaxy	RA (J2000)	Dec. (J2000)	cz (km s^{-1})	Distance (Mpc)	L_{IR} [b] (10^{10} L$_\odot$)	Telescope	Reference[c]
M 82	09:55:53.1	+69:40:41	203	3.9	5.8	SMT/IRAM	1
NGC 3079	10:01:57.9	+55:40:51	1166	16.1	5.4	SMT/IRAM	2
NGC 3504	11:03:11.2	+27:58:21	1525	8.1	5.2	SMT	3
IC 694	11:28:27.3	+58:34:43	3100	47.7	32	IRAM	4
NGC 4418	12:26:54.7	−00:52:42	2179	29	12	SMT	5
Mrk 231	12:56:14.2	+56:52:25	12139	175	324	IRAM	6
NGC 6240	16:52:58.9	+02:24:03	7200	98	71	SMT/IRAM	7
NGC 6946	20:34:52.3	+60:09:14	40	5.5	1.4	SMT	8

Notes: [a]The position (in Equatorial *J*2000 coordinates) and heliocentric radial velocities were taken from NED.[2]
[b]Total IR luminosities from Sanders et al. (2003).
[c]The distance of each source is from 1: Sakai & Madore (1999); 2: Tsai & Hwang (2015); 3: Elmegreen et al. (1997); 4: Sanders et al. (2003); 5: Spoon et al. (2001); 6: Lindberg et al. (2016); 7: Zhang et al. (2012); 8: Pan et al. (2015).

resolutions of ∼ 20–40 km s^{-1}. The velocity-integrated intensities of these lines were derived from single component Gaussian fit to the spectra, or integrated over the full width to zero power, if the line profiles significantly deviated from a Gaussian profile. Tables B1–B6 present the line parameters.

In order to check the noise level at different frequency channels for each source among several GHz bandwidths, we used all the individual spectra after resampling and smoothing to the final velocity resolution, which were used for the final-averaged spectrum. Since each source has many spectra, that is, each channel would have many observed value. Then, we do statistics with data for each channel to obtain the averaged value, as final spectrum, and rms (noise), which are shown in Figs C1–C5. The generally result is that the noise levels do not vary much among the frequency coverage. As an example, the noise spectrum of NGC 3079 in the 3-mm band is shown in Appendix D.

3 RESULTS

In Figs 1–6, we present the spectra of rare isotopologues of dense gas tracers towards these extragalactic objects. The stronger molecular emission lines, HCN J = 3–2 and 1–0, HCO$^+$ J = 1–0, and HNC J = 1–0, are overlaid for comparison. Lines with velocity-integrated intensities above the 3σ level are considered as detections. We also estimate the 3σ upper limits for the velocity-integrated intensity of the undetected lines. Detailed line parameters of each galaxy is presented in Appendix B, including central velocity, line widths, and velocity-integrated intensity.

3.1 Detections of isotopologues

3.1.1 H^{13}CN 3–2 observations with the SMT 10-m telescope

With the SMT 10-m telescope, the H^{13}CN 3–2 line is detected in four sources: M 82, NGC 3079, NGC 4418, and NGC 6240. We estimated the upper limits for the other two sources: NGC 6946 and NGC 3504. This is the first detection of H^{13}CN J = 3–2 in a sample of several external galaxies. The spectra of H^{13}CN J = 3–2 are shown in panel (a) of Figs 1–6.

H^{13}CN 3–2 emission is located within the velocity range of HCN 3–2 emission in all of the sources. HCN 3–2 emission shows two distinguishable velocity components in NGC 3079, which is consistent with the results in the literature of Pérez-Beaupuits, Aalto & Gerebro (2007). H^{13}CN 3–2 emission in NGC 3079 only shows the blueshifted component of HCN 3–2. Two velocity components of HCN 3–2 are also observed in M 82, and H^{13}CN 3–2 is dominated by the blueshifted component of HCN 3–2. Both HCN and H^{13}CN 3–2 show a single velocity component in NGC 4418 and NGC 6240. The line width of H^{13}CN 3–2 is 89.8 km s^{-1}, which is narrower than the 222 km s^{-1} estimated by HCN 3–2 in NGC 6240.

3.1.2 H^{13}CN 1–0 and other isotopic lines observed with the IRAM 30-m telescope

The spectra of rare isotopologues of dense gas tracers in the 3-mm band, including H^{13}CN 1–0, HC^{15}N 1–0, H^{13}CO$^+$ 1–0, HN^{13}C 1–0, and H^{15}NC 1–0, towards five galaxies are shown in Figs 1–5. To better demonstrate the significance of the various detections and tentative detections, the broad-band 3 mm spectra are presented in Appendix C. The H^{13}CN 1–0 line is detected in four sources (M 82, NGC 3079, Mrk 231, and NGC 6240), while only an upper limit of the velocity-integrated intensity for this line is given for IC 694. We compare these isotopologues of dense gas tracers, in the J = 1–0 and 3–2 transitions, based on that the beam sizes of the two telescopes are almost the same for our observations.

The detailed information for each source is listed below:

M 82: H^{13}CN, H^{13}CO$^+$, and HN^{13}C 1−0 are detected in this source. Although H^{13}CN and H^{13}CO$^+$ had been reported by Aladro et al. (2015), who also used the IRAM 30-m telescope, there were large uncertainties in estimating the velocity-integrated intensities of these lines, with a fixed line width of 100 km s^{-1} and centre velocity of 300 km s^{-1}. With about a factor of 2 higher sensitivity, our data can not only better derive the velocity-integrated intensities, but also are useful for a comparison of the line profiles with simultaneously obtained main isotopologues. This is the first report of HN^{13}C 1–0 detection in M 82. As shown in panels (d) and (h) of Fig. 1, due to blending, HC^{15}N 1–0 and H^{15}NC 1–0 are hard to distinguish from SO 2–1 and CH_3CH_2CN $27_{3,24}$-$27_{2,25}$, respectively. However, the redshifted part of the emission feature near 86055 MHz should be from HC^{15}N (see panel c in Fig. 1), because there is no related HCN 1–0 emission at the same velocity range if it is identified as SO 2–1. It is the similar case for the blueshifted part of the emission feature near the frequency of H^{15}NC 1–0 (panel g in Fig. 1).

H^{13}CN 1–0 and 3–2 line profiles differ from each other (see panels a and b of Fig. 1). All identified isotopic lines of the J = 1–0 transition are dominated by the redshifted component of HCN 1–0

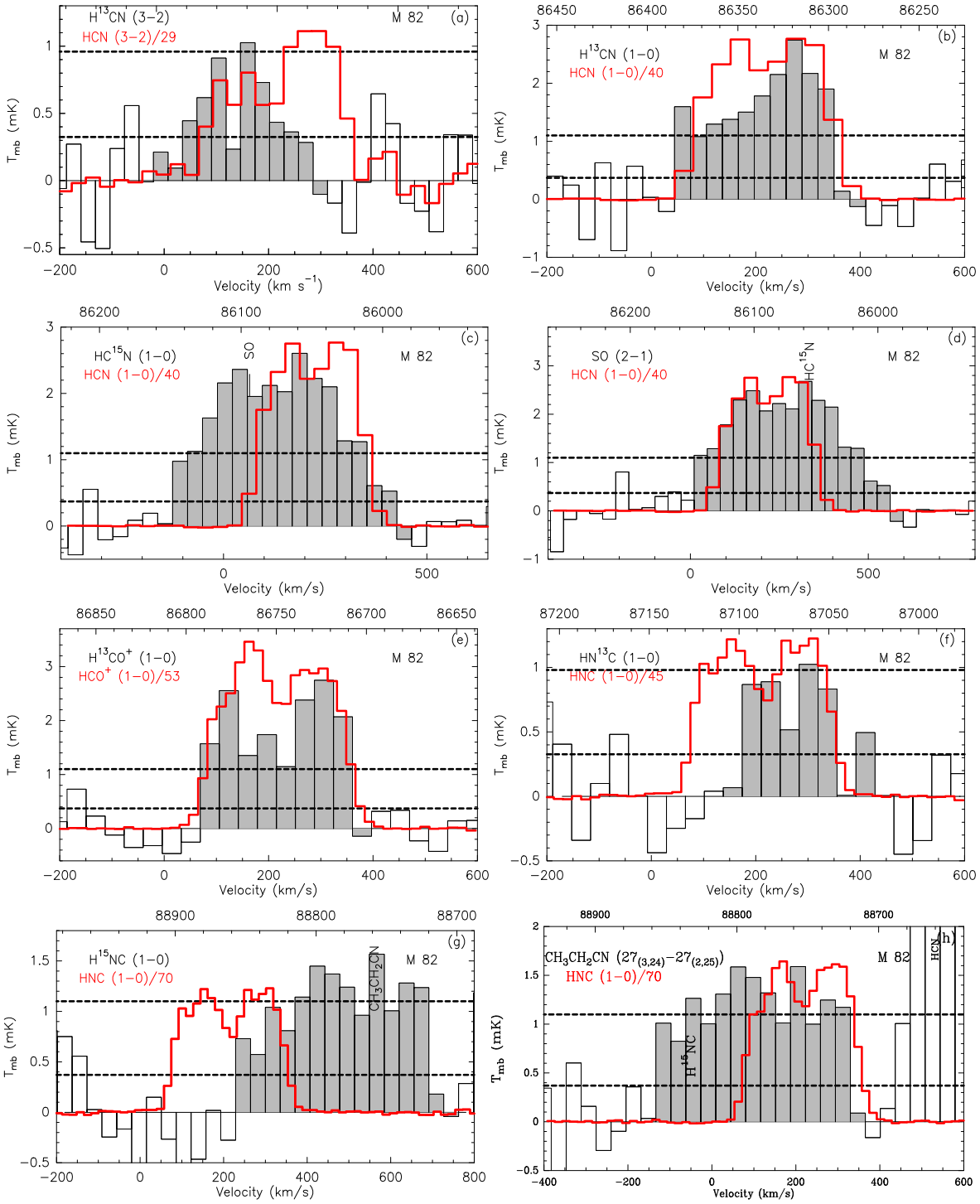

Figure 1. Lines detected in M 82. Dashed lines are 1σ and 3σ noise levels derived from first-order baseline fitting. The grey-filled black spectra shown in each subfigure are identified as the line noted in black at the top left. The velocity resolution is 36 km s^{-1} for all molecules. Due to blending, $HC^{15}N$ 1–0 and $H^{15}NC$ 1–0 are hard to distinguish from SO 2–1 and CH_3CH_2CN $27_{3,24}$-$27_{2,25}$ (in panels c and g), respectively. While, the panels d and h show that the emission redshift of the $HC^{15}N$ line centre is solely from $HC^{15}N$, and the emission blueshift of the $H^{15}NC$ line centre is $H^{15}NC$.

in panels (b), (c), and (f) of Fig. 1, while $H^{13}CN$ 3–2 is dominated by the blueshifted component. A wide-band spectrum of M 82 is shown in Fig. C1. Note that the components 1 and 2 might be from the molecular gas outflow traced by HCO^+ (Kepley et al. 2014); components 3 and 4 may be from the outflowing gas traced by HCN or from both CH_3CH_2CN and CH_3OCHO emissions. We classify the emission feature at approximately 87856 MHz as an unidentified line for component 5.

NGC 3079: two isotopic lines of dense gas tracers: $H^{13}CN$ 1–0 and $H^{13}CO^+$ 1–0, are detected in NGC 3079. Redshifted component of $HC^{15}N$ 1–0 is tentatively detected at $\sim 3\sigma$ level, while only upper limit of the blueshifted component is obtained. The observational

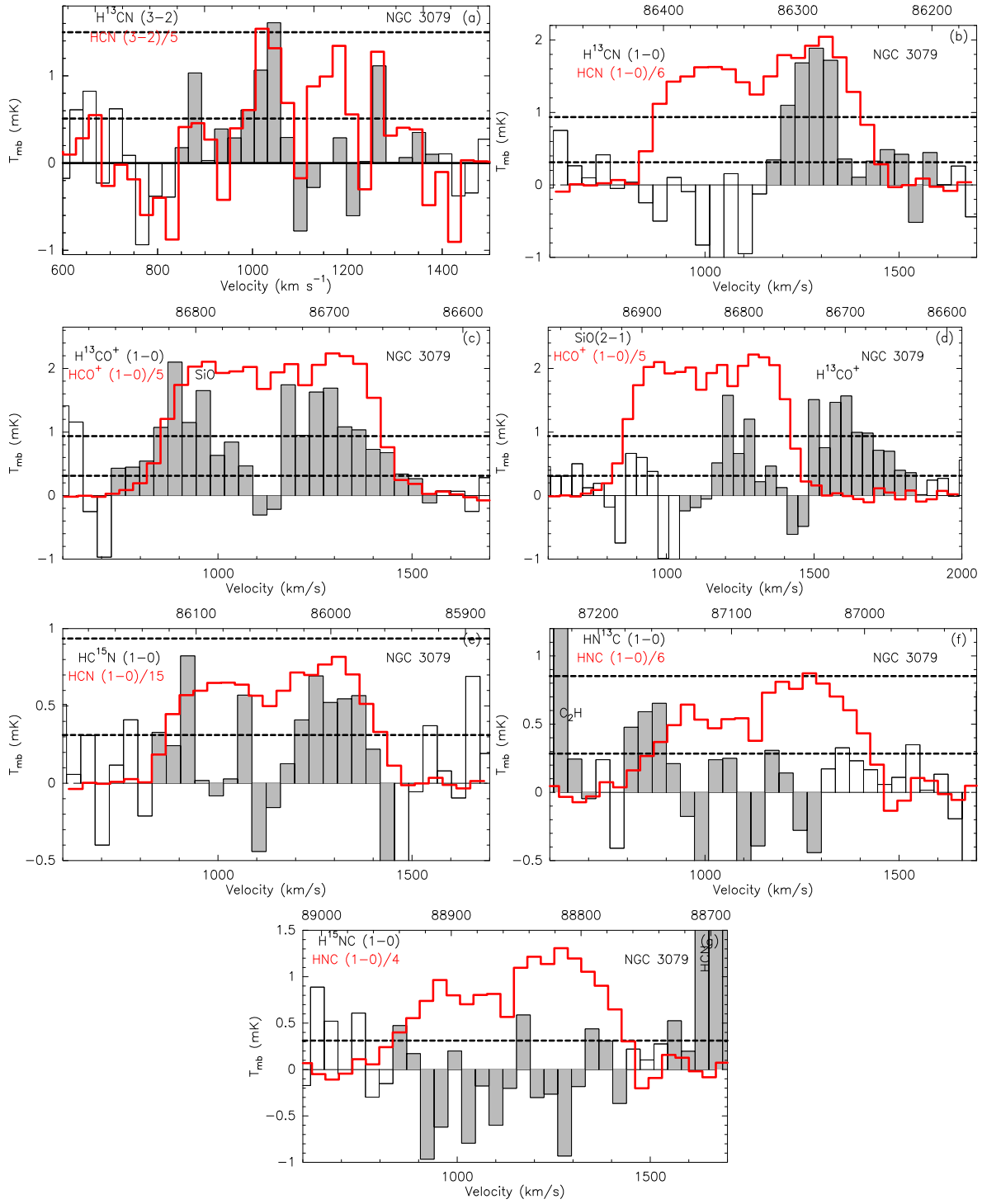

Figure 2. Lines detected in NGC 3079. Dashed lines are 1σ and 3σ noise levels derived from the first-order baseline fitting. The grey-filled black spectra shown in each subfigure are identified as the line noted in black at the top left. The upper limits of $HN^{13}C$ and $H^{15}NC$ $J = 1$–0 are obtained without significant emission features, as shown in panels (f) and (g). The velocity resolution is 36 km s^{-1} for all molecules.

sensitivities of $H^{13}CO^+$ 1–0 and $H^{13}CN$ 1–0 are two times better than those of Costagliola et al. (2011). These three isotopologues are dominated by the red-shifted component of HCN 1–0 as shown in panels (b), (c), and (e) of Fig. 2. However, $H^{13}CN$ 3–2 is dominated by the blueshifted component of HCN 3–2 (panel a of Fig. 2). The different line profiles of $H^{13}CN$ 3–2 and 1–0 indicate that the blueshifted component gas traced by HCN 1–0 is likely warmer and denser than that of the redshifted gas in NGC 3079, which is similar to the condition encountered in M 82. The upper limits of $HN^{13}C$ and $H^{15}NC$ $J = 1$–0 are obtained.

IC 694: Upper limits of the integrated intensity for each isotopologue were derived and summarized in Table B6. The main isotopologues of HCN, HCO^+, and HNC 1–0 are detected, which is consistent with the results reported by Jiang, Wang & Gu (2011).

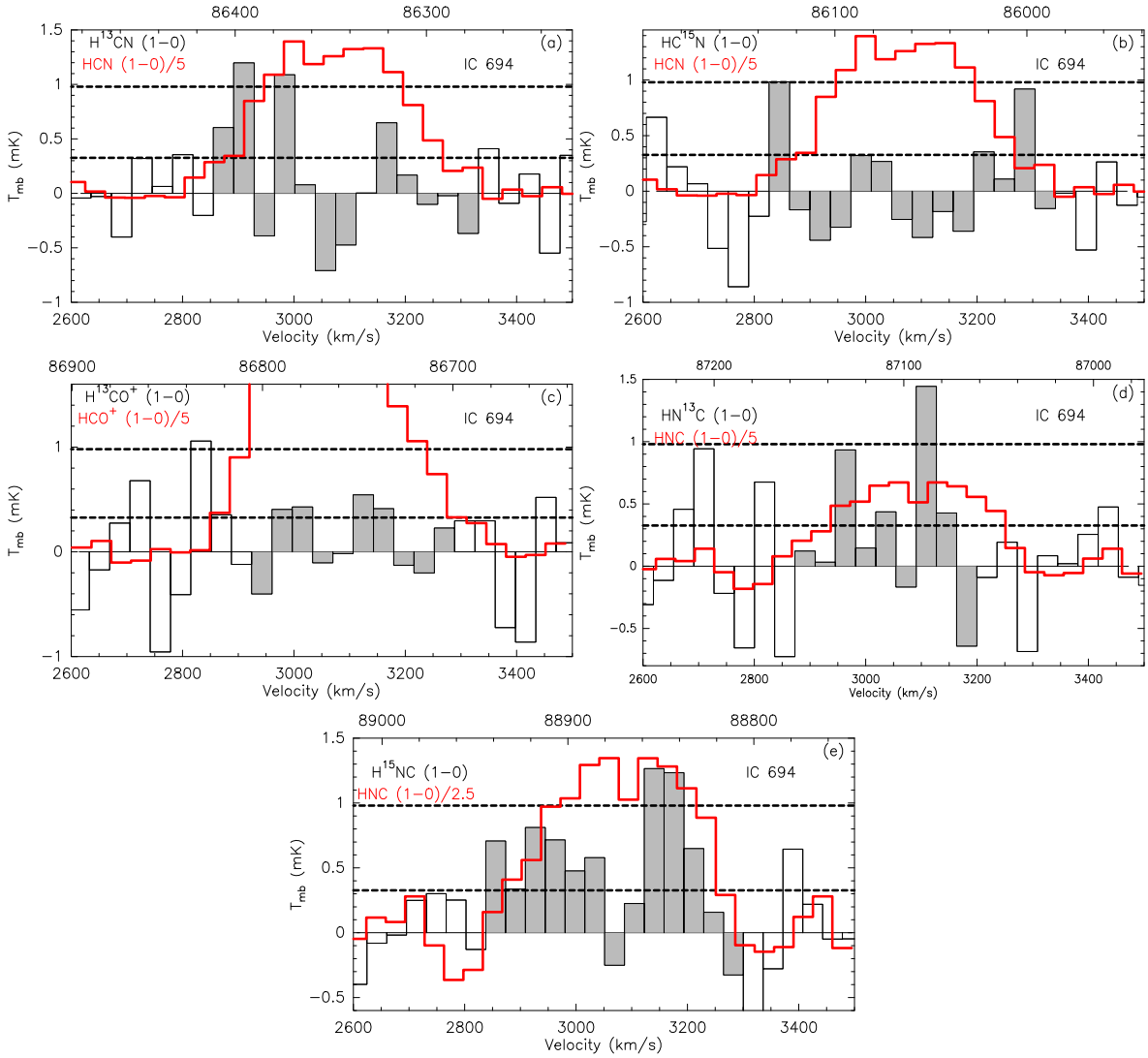

Figure 3. Although no isotopic lines of dense gas tracers are detected in IC 694, upper limits of the integrated intensity are derived for each isotopologues. So we show the measured spectra lines in IC 694. Dashed lines are 1σ and 3σ noise levels derived from the first-order baseline fitting. The grey-filled black spectra shown in each subfigure are identified as the line noted in black at the top left. The velocity resolution is 36 km s^{-1} for all molecules.

Mrk 231: $H^{13}CN$ 1–0 and $HC^{15}N$ 1–0 are detected and we have a tentative detection of $H^{13}CO^+$ 1–0 in Mrk 231. The fluxes of $H^{13}CN$ 1–0 and $HC^{15}N$ 1–0 are consistent with those in Lindberg et al. (2016), which were observed with the IRAM Plateau de Bure Interferometer (PdBI). While, it is lower than the result of Costagliola et al. (2011), although our detected line width of $H^{13}CN$ is similar to their result. The 3σ upper limits of the $HN^{13}C$ and $H^{15}NC$ 1–0 intensities are estimated, and shown in Table B6. A wide-band spectrum of this source is shown in Fig. C4.

NGC 6240: there is a 4σ level emission feature around 86340 MHz. If the emission feature is identified as $H^{13}CN$ 1–0, the central velocity of $H^{13}CN$ 1–0 would deviate from that of HCN 1–0 by approximately +200 km s^{-1}, although it is still within the velocity range of HCN 1–0 (see Section 4.1 for a detailed discussion). $H^{13}CN$ 1–0 of NGC 6240 was marginally detected by Tunnard et al. (2015) with the IRAM PdBI and Manohar & Scoville (2017) with the Combined Array for Research in Millimeter-wave Astronomy, without velocity informations in both papers.

The 3σ upper limits for both $HN^{13}C$ and $H^{15}NC$ 1–0 are estimated. $HC^{15}N$ 1–0 is outside the covered frequency range. There is an emission feature, which can be identified as SiO 2–1, while no significant emission feature can be identified as $H^{13}CO^+$ 1–0 (see panels e and f of Fig. 5).

3.2 Optical depth

With the assumption of the same filling factors and excitation temperatures, the averaged optical depth of each isotopologue can be estimated using

$$R = \frac{1 - e^{-\tau_{12}}}{1 - e^{-\tau_{13}}} \quad (1)$$

where R is the ratio of the measured velocity-integrated intensities, which are listed in Table 2. For comparison, we test three values for $^{12}C/^{13}C$ and $^{14}N/^{15}N$ abundance ratios to estimate the optical depths, which are also listed in Tables 3 and 4. The $^{12}C/^{13}C$ abundance ratio was suggested to be 40 in nearby galaxies (Henkel

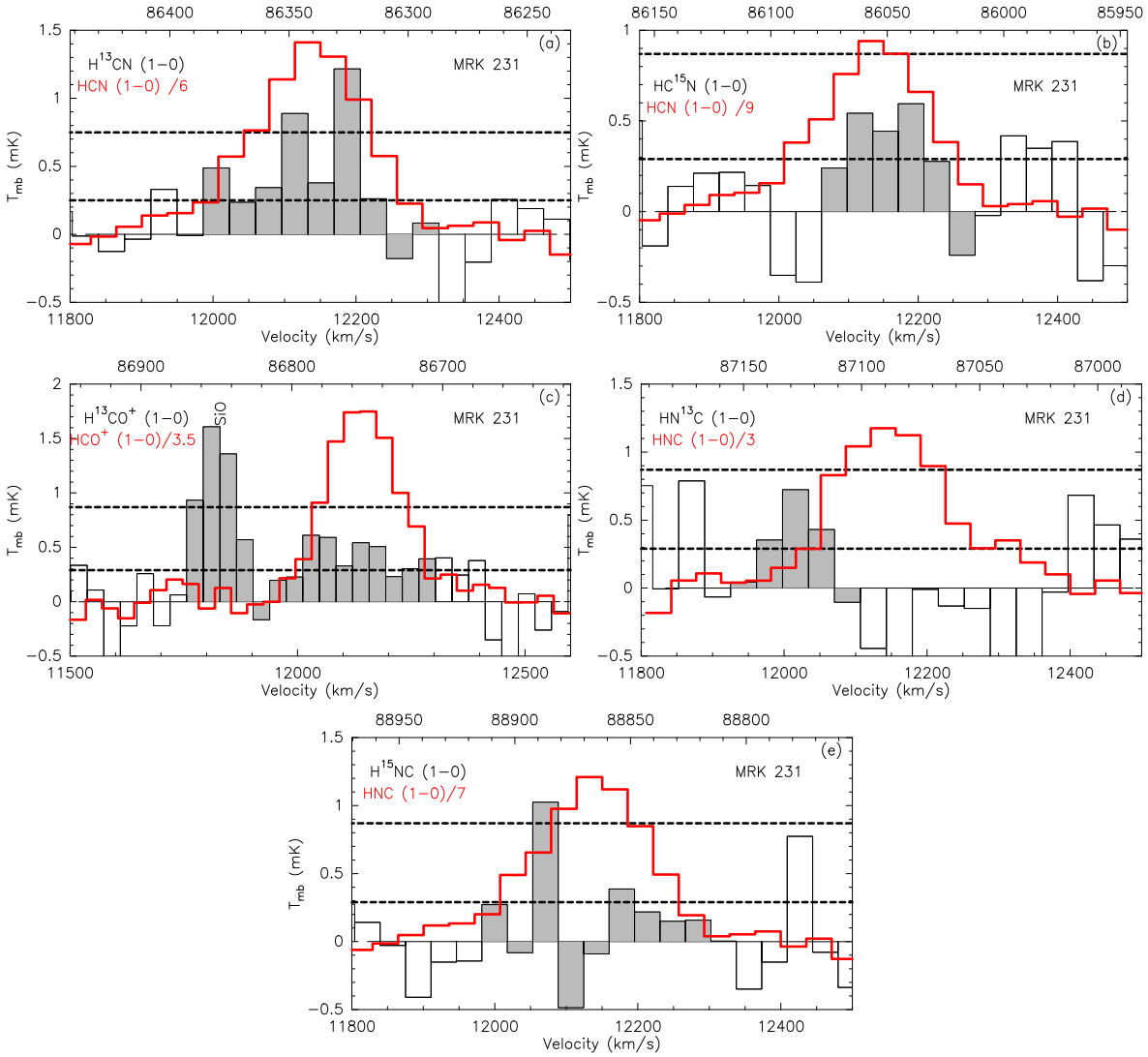

Figure 4. Lines detected in Mrk 231. Dashed lines are 1σ and 3σ noise levels derived from the first-order baseline fitting. The grey-filled black spectra shown in each subfigure are identified as the line noted in black at the top left. $H^{13}CO^+$ 1–0 is only detected about 2σ level in panel (c). The 3σ upper limits for $HN^{13}C$ and $H^{15}NC$ 1–0 intensity are estimated from panels (d) and (e). The velocity resolution is 36 km s^{-1} for all molecules.

et al. 1998), 89 in the Solar system (Clayton & Nittler 2004), and 200 in ultraluminous infrared galaxies (ULIRGs) (Romano et al. 2017). In addition, the $^{14}N/^{15}N$ abundance ratios were assumed to be 100, 200, and 290, which are from an investigation of Large Magellanic Cloud (Chin et al. 1999), massive star-forming regions (Li et al. 2017), and the local interstellar medium (Adande & Ziurys 2012).

For all dense gas tracers (HCN, HCN, HCO^+ 1–0, and HCN 3–2), their optical depths show a large variation in different types of galaxies, which indicates that there are large uncertainties in estimating dense gas masses using only the measured luminosity of dense gas tracers. We find that the optical depths of the main isotopologues are high to moderate in ULIRG Mrk 231, NGC 6240, and LIRG NGC 4418. For M 82 and NGC 3079, the optical depths of HCN 1–0 and 3–2 in the two velocity components are different. The blueshifted part of HCN 1–0 is obviously optically thin. While, it is obviously optically thin in the redshifted part of HCN 3–2 (see Table 3). The optical depth of HCN 3–2 is higher than that of HCN 1–0 in the galaxies with detections of both HCN 1–0 and 3–2, which indicates that ground state transitions of dense gas tracers might better trace the star formation than mid-*J* transitions.

In Table 2, the uncertainties of fluxes caused by absolute flux calibration and the pointing error of the telescope might affect the ratio of $HCN/H^{13}CN$ 3–2, since two lines are observed during different days with the SMT 10-m telescope. On the other hand, for the IRAM 30-m telescope data, due to the species in the $J = 1$–0 transition are simultaneously observed, the ratios of dense gas tracers and their isotopic lines in the $J = 1$–0 transition would not be affected by the uncertainties of fluxes.

3.3 Population diagnosis

We present a population diagram analysis for $H^{13}CN$, which include two transitions detected in M 82, NGC 3079, NGC 4418, and NGC 6240. Note that the line parameters of the $H^{13}CN$ $J = 1$–0 transition in NGC 4418 are from Costagliola et al. (2015). Since $H^{13}CN$ line is optically thin, LTE is assumed to calculate its column

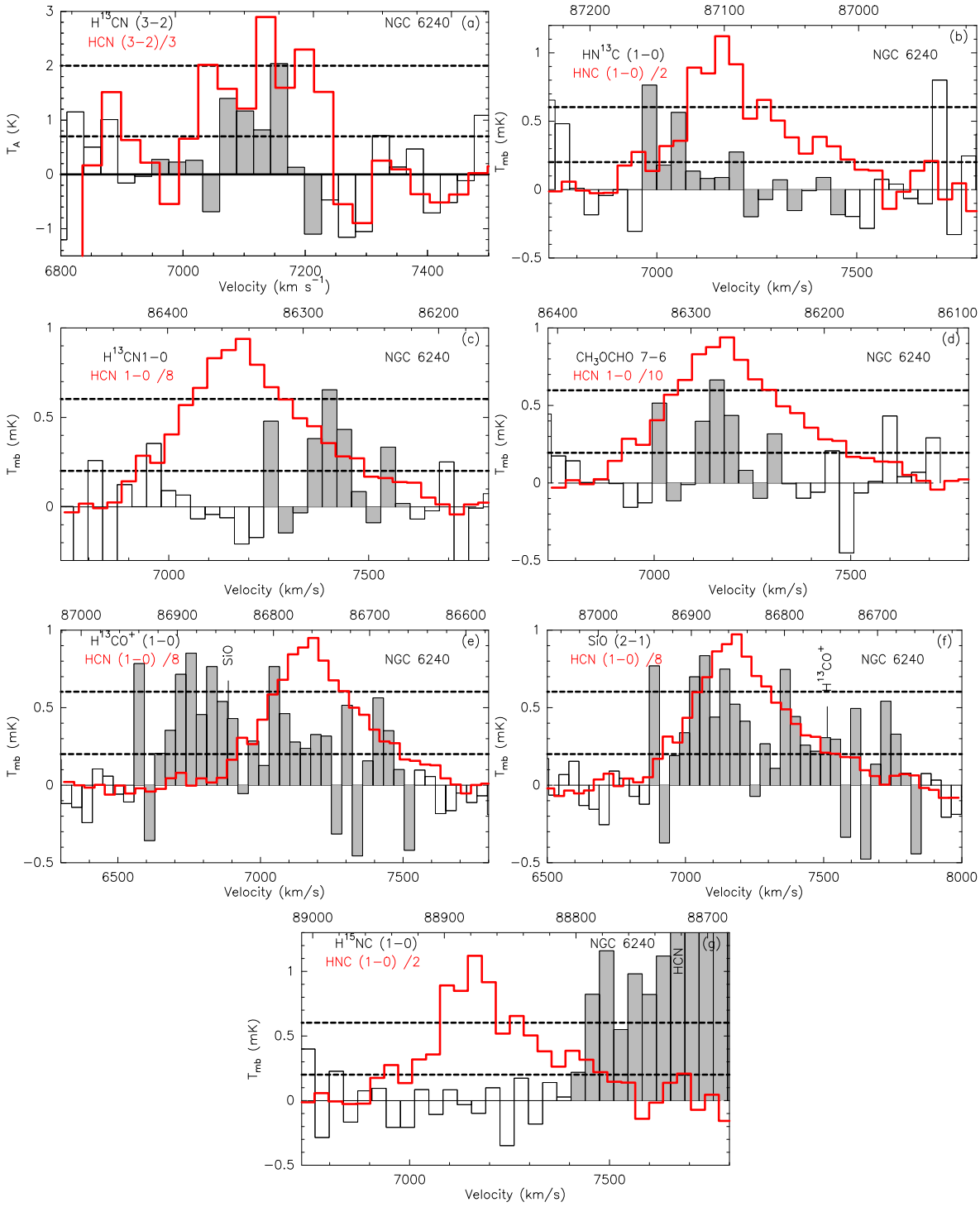

Figure 5. Lines detected in NGC 6240. Dashed lines are 1σ and 3σ noise levels derived from the first-order baseline fitting. The grey-filled black spectra shown in each subfigure are identified as the line noted in black at the top left. $HC^{15}N$ 1–0 is not covered by the observed frequency range. $H^{13}CO^+$ is overlaid with the HCN (red) emission, as HCO^+ 1–0 was not covered by this observation. The velocity resolution is 36 km s^{-1} for all molecules.

density (N) and the excitation temperature. For each rotational transition, following the Boltzmann diagram method (Goldsmith & Langer 1999), we can write the column density of the upper energy state as

$$N_u = \frac{8\pi k \nu^2 W}{hc^3 A_{u\ell}} \qquad (2)$$

where N_u is the upper state column density of the molecule, W is the integrated brightness temperature, k is the Boltzamann constant, ν is the frequency of the transition, h is the Planck constant, and $A_{u\ell}$ is the Einstein transition probability coefficient. The spectroscopic parameters were obtained from the Cologne Database for Molecular Spectroscopy (CDMS; Müller et al. 2005) and JPL catalogues (Pickett et al. 1998). The column densities of these

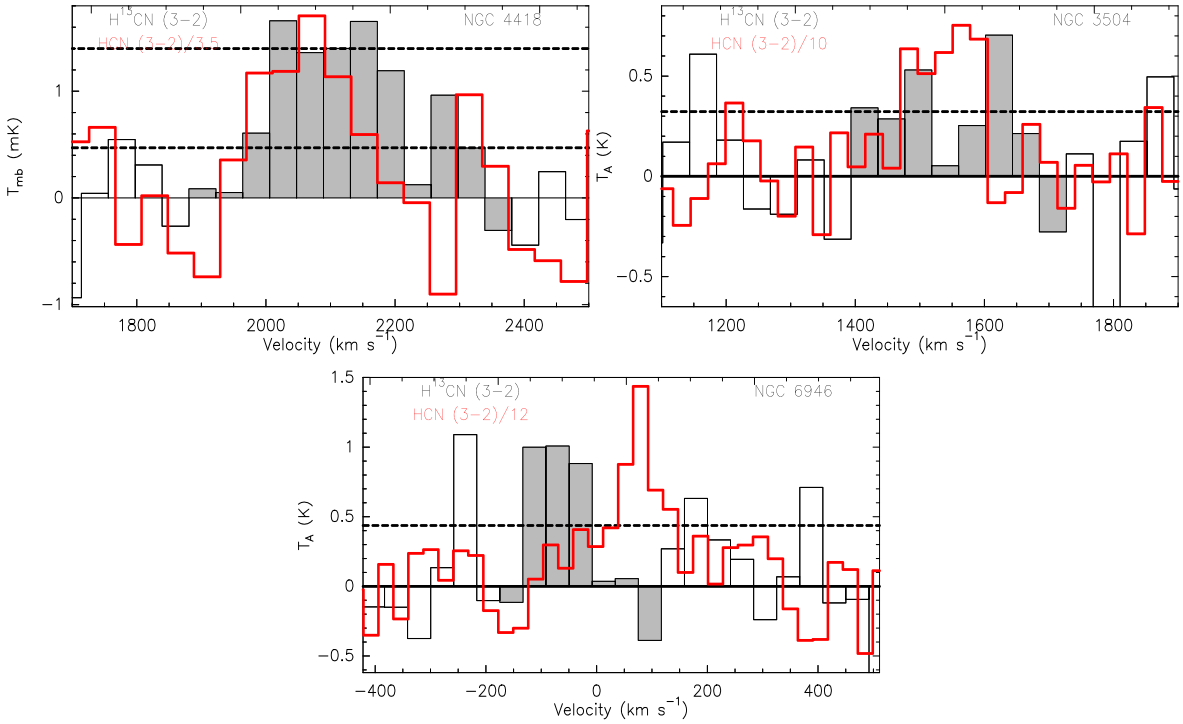

Figure 6. $H^{13}CN$ 3–2 (grey-filled area) overlaid with HCN 3–2 (red line) emission in three galaxies (NGC 4418, NGC 3504, and NGC 6946). $H^{13}CN$ 3–2 emission is considered for the detection in NGC 4418, while only upper limits are obtained in NGC 3504 and NGC 6946. The dashed lines are 1σ and 3σ noise levels derived from first-order baseline fitting. The velocity resolution is 36 km s^{-1} for all molecules.

Table 2. Isotopic line intensity ratios for HCN, HNC, and HCO^+.

Galaxy	$\frac{HCN}{H^{13}CN}$ 1–0	$\frac{HCN}{H^{13}CN}$ 3–2	$\frac{HCN}{HC^{15}N}$ 1–0	$\frac{HCO^+}{H^{13}CO^+}$ 1–0	$\frac{HNC}{HN^{13}C}$ 1–0	$\frac{HNC}{H^{15}NC}$ 1–0	$\frac{H^{13}CN}{HC^{15}N}$ 1–0
M 82	40 ± 3.6^a	13 ± 3.1^b	–	52 ± 7.8^a	37 ± 6.5^a	–	–
NGC 3079	10 ± 4.5^a	10 ± 2.0^b	30 ± 9.1^a	7.0 ± 1.6^a	>27.5	>22	>1.7
NGC 3504	–	>12.9	–	–	–	–	–
IC 694	>11	–	>11	>17.5	>7.1	>4.3	–
NGC 4418	7.6 ± 2.8	4.0 ± 0.73	–	–	–	–	>4
Mrk 231	16 ± 4.8	–	23 ± 6.5	12 ± 4.8	>7	>7	1.4 ± 0.58
NGC 6240	>45	11.3 ± 4.3	–	–	>10.5	>7.5	–
NGC 6946	–	>18.8	–	–	–	–	–

Notes: M 82 and NGC 3079 show a double-pecked structure for the main isotopologues. We only calculate the peck intensity ratio of the higher velocity range for $J = 1$–0 transition and the peck intensity ratio of the lower velocity range for $J = 3$–2 transition. The line ratio of $HCN/H^{13}CN$ 1–0 in NGC 4418 is obtained with IRAM 30-m telescope from the literature: Costagliola et al. (2011).
[a] is the line ratio at the line peck of the higher velocity range and [b] is the line ratio at the line peck of the lower velocity range. Due to 3σ upper limits of intensity are estimated for some isotopologues, lower limits are shown for their isotopic line ratios.

species are estimated with the following equation (Watanabe et al. 2014):

$$N = \frac{N_u Q(T_{ex})}{g_u e^{-E_u/T_{ex}}} \left(\frac{T_{ex}}{T_{ex} - T_{bg}} \right) \quad (3)$$

where N is the column density of molecules, $Q(T_{ex})$ is the partition function, g_u is the degeneracy of the upper state, and E_u is the upper level energy. The partition function $Q(T_{ex})$ of each molecule is calculated by interpolating the partition function at different temperatures taken from the CDMS.

The data are corrected by the beam dilution effect as $T_B = [(\theta_s^2 + \theta_b^2)/\theta_s^2] \times T_{MB}$, where T_B is the source average brightness temperature, θ_s is the source size, θ_b is the beam size in arcseconds, and T_{MB} is the measured main beam temperature. Based on interferometric observations of ^{12}CO, HCO, and $H^{13}CO^+$ for M 82 (García-Burillo et al. 2002; Fuente et al. 2008), CO (1–0) for NGC 6240 (Feruglio et al. 2013), CO (1–0) for NGC 3079 (Koda et al. 2002), and HCN for NGC 4418 (Costagliola et al. 2015), we roughly assumed source sizes of 12 and 2 arcsec for M 82 and NGC 6240 and 11 and 0.4 arcsec for NGC 3079 and NGC 4418, respectively.

The derived excitation temperatures are from 10 to 25 K and column densities are about 10^{10} cm^{-2} in these four sources (see Table 5). Note that both the excitation temperatures and the column densities are beam-averaged values. Given the uncertainty on the source size and beam filling factor, the derived column densities should be considered as lower limits to the real value. The beam-averaged low excitation temperatures in these sources indicate that at least a part of the dense molecular gas is not thermalized up to $J = 3$ for $H^{13}CN$.

Table 3. Optical depths for HCN.

Galaxy	τ(HCN)[a] (1–0)			τ(HCN)[b] (1–0)			τ(*HCN*) (3–2)			Velocity components
	40[c]	89[c]	200[c]	100[d]	200[d]	290[d]	40[c]	89[c]	200[c]	
M 82	$<<1$	0.6 ± 0.01	2.8 ± 0.7	–	–	–	3.4 ± 0.7	7.1 ± 1.5	16.0 ± 3.2	1
	<1	1.9 ± 0.3	5.0 ± 0.5	–	–	–	–	–	–	2
NGC 3079	$<<1$	–	–	<0.4	<2.5	<6.4	4.1 ± 0.7	9.4 ± 1.7	21.1 ± 3.6	1
	<1	9.4 ± 3.1	21.1 ± 7.0	3.2 ± 0.9	6.8 ± 1.7	9.8 ± 2.3	–	–	–	2
NGC 3504	–	–	–	–	–	–	<3.1	<7.2	<16.1	1
IC 694	<3.7	<8.5	<19	<9.5	<19.1	27.4	–	–	–	1
NGC 4418	5.6 ± 1.5	12.6 ± 3.7	28.2 ± 8.0	–	–	–	11.5 ± 2	25.6 ± 4.5	57.5 ± 10	1
Mrk 231	2.3 ± 0.8	5.7 ± 1.4	12.9 ± 3.1	4.4 ± 1.1	8.9 ± 2.1	12.9 ± 2.9	–	–	–	1
NGC 6240	<1	<1.6	<4.4	–	–	–	3.6 ± 1.2	8.2 ± 2.4	18.5 ± 5.3	1
NGC 6946	–	–	–	–	–	–	<1.8	<4.8	<10.9	1

Notes: For M 82 and NGC 3079, components 1 and 2 are the two Gaussian components for the HCN, HCO^+, and HNC 1–0, respectively. While, all other sources show a single velocity component. The upper limits are $<3\sigma$.
[a]The optical depth of HCN is calculated by the ratio of HCN/$H^{13}CN$.
[b]The optical depth of HCN is calculated by the ratio of HCN/$HC^{15}N$.
[c]40 (nearby galaxies, Henkel et al. 1998), 89 (Solar system, Clayton & Nittler 2004), and 200 (ULIRGs, Romano et al. 2017) are $^{12}C/^{13}C$ ratios.
[d]100 (nearby starburst galaxies, Chin et al. 1999), 200 (massive star-forming regions, Li et al. 2017), and 290 (local interstellar medium, Adande & Ziurys 2012) are $^{14}N/^{15}N$ ratios.

Table 4. Optical depths for HNC and HCO^+.

Galaxy	τ(HNC)[a] (1–0)			τ(HNC)[b] (1–0)			τ(HCO^+) (1–0)		
	40[c]	89[c]	200[c]	100[d]	200[d]	290[d]	40[c]	89[c]	200[c]
M 82	0.16 ± 0.01	2.2 ± 0.5	5.5 ± 0.9	–	–	–	<1	1.2 ± 0.3	3.8 ± 0.6
NGC 3079	<0.83	<3.15	<7.4	<1.4	<4.1	<9.3	6.2 ± 1.1	13.7 ± 2.7	30.8 ± 6.1
NGC 3504	–	–	–	–	–	–	–	–	–
IC 694	<6.5	<13.5	<30.3	<10.6	<23.6	52.9	<2.0	<5.2	<11.8
NGC 4418	–	–	–	–	–	–	–	–	–
Mrk 231	<6.2	<13.7	<30.8	<6.2	<13.7	<30.8	3.4 ± 1.2	7.7 ± 2.3	17.4 ± 5.1
NGC 6240	<3.9	<8.9	<20.0	<5.7	<12.7	<26.8	–	–	–
NGC 6946	–	–	–	–	–	–	–	–	–

Notes: For M 82 and NGC 3079, we just show optical depth of the redshift component for HNC and HCO^+. [a]The optical depth of HCN is calculated by the ratio of HNC/$HN^{13}C$. [b]The optical depth of HCN is calculated by the ratio of HNC/$H^{15}NC$. [c], [d] are the same as Table 3 but for the optical depths of HNC and HCO^+. The upper limits are $<3\sigma$.

Table 5. Column densities and excitation temperature of $H^{13}CN$ in M 82, NGC 3079, NGC 6240, and NGC 4418.

Galaxy	$N(H^{13}CN)$ (cm^{-2})	$T_{ex}(H^{13}CN)$ (K)
M 82	$(4.5 \pm 0.4) \times 10^{10}$	10.6 ± 1.2
NGC 3079	$(2.5 \pm 0.4) \times 10^{10}$	10.1 ± 1.7
NGC 4418	$(4.2 \pm 0.9) \times 10^{10}$	25.0 ± 0.5
NGC 6240	$\geq 6.7 \times 10^{9}$	≥ 20.0

3.4 $^{14}N/^{15}N$ ratios

Since the intensity ratio $I(H^{13}CN)/I(HC^{15}N)$ in NGC 3079 and Mrk 231 are directly linked to the abundance ratios of these molecules, we can estimate the $^{14}N/^{15}N$ abundance ratio, with the so-called double isotope method (Adande & Ziurys 2012). We assume abundance ratio of $^{12}C/^{13}C = 40$ for NGC 3079 (Henkel et al. 1998) and 100 for Mrk 231 (Henkel et al. 2014). These two galaxies display a low $^{14}N/^{15}N$ abundance ratio. This ratio is much lower than that in the local interstellar medium of 290 (Adande & Ziurys 2012) and 270 in our Solar system (Dahmen, Wilson & Matteucci 1995).

4 DISCUSSION

4.1 Line identification

M 82: the spectra of $HC^{15}N$ 1–0 and $H^{15}NC$ 1–0 are seriously affected by the contamination from SO 2–1 and CH_3CH_2CN $27_{3,24}$-$27_{2,25}$, respectively. Even though SO and CH_3CH_2CN contribute these two emissions, if these two emission features are identified as SO and CH_3CH_2CN, there will be some emissions outside of the velocity range of HCN 1–0, as shown in panels (d) and (h) of Fig. 1. Although we do not treat the $HC^{15}N$ 1–0 and $H^{15}NC$ 1–0 as detections for discussion of dense gas properties, the high velocity components of the emission at approximately 86055 MHz should be $HC^{15}N$ 1–0 and the low velocity components of another emission at approximately 88865 MHz should be $H^{15}NC$ 1–0. $HN^{13}C$ 1–0 is detected at about a 5σ level, within the velocity range of HNC 1–0 (panel f in Fig. 1). This is the first report of $HN^{13}C$ 1–0 detection in M 82.

NGC 3079: although HCN 1–0 is detected in two velocity components, all the isotopologues of dense gas are detected in only one velocity component. These two isotopologues are dominated by the redshifted component of HCN 1–0 in panels (b), (c) and (e) of Fig. 2. However, $H^{13}CN$ 3–2 is dominated by the blueshifted component of HCN 3–2 (see panel a in Fig. 2). Both $H^{13}CO^+$ 1–0

and SiO 2–1 are detected in NGC 3079. From the panels (c) and (d) of Fig. 2, if $H^{13}CO^+$ 1–0 and SiO 2–1 only show their redshifted component, the high velocity component must be $H^{13}CO^+$ 1–0 and the low velocity component should be SiO 2–1.

NGC 4418: the data of molecular species in the 3-mm band are taken from the literature (Costagliola et al. 2011, 2015). $H^{13}CN$ 1–0 has been detected with the IRAM 30-m telescope (Costagliola et al. 2011) and the ALMA (Costagliola et al. 2015). While, $HC^{15}N$ 1–0 and $H^{15}NC$ 1–0 were not detected in Costagliola et al. (2015). With the noise level of $H^{13}CN$ 1–0 and the width of HCN 1–0 and HNC 1–0, we estimate the 3σ upper limit of flux densities for $HC^{15}N$ 1–0 and $H^{15}NC$ 1–0, which are 0.17 and 0.15 Jy km s^{-1}, respectively. The lower limit of the ratio of $H^{13}CN/HC^{15}N$ is found to be 4 (Costagliola et al. 2015), which implies that the $^{14}N/^{15}N$ abundance ratio should exceed 200 with the assumption of $^{12}C/^{13}C$ as 40 (Henkel et al. 1998) using the so-called double-isotope method (Adande & Ziurys 2012).

The line width, peak intensity, as well as velocity-integrated intensity of HCN 3–2 in our observation are consistent with those detected by Costagliola et al. (2015), applying a conversion factor of $S/T_{mb} = 60$ Jy K^{-1}. On the other hand, the velocity-integrated intensity of HCN 3–2 is approximately a factor of 5 higher than that in Aalto, Monje & Martín (2007) observed with the IRAM 30-m telescope, which may be caused by pointing error of the telescope during there observation. Although the line width of $H^{13}CN$ 3–2 is about 30 km s^{-1} broader than HCN 3–2, it is similar to that of HC_3N 10–9 reported by Costagliola et al. (2011). The line ratio of $H^{13}CN$ 3–2/1–0 is close to unity, which is similar to that of Arp 220 (Wang et al. 2016). This indicates that these two galaxies might have similar excitation temperatures and densities of dense molecular gas.

Mrk 231: $H^{13}CN$ and $HC^{15}N$ 1–0 detections were reported by Lindberg et al. (2016), which is consistent with our results. However, no scientific analysis or discussion was made in that paper, which was mainly focused on molecular outflows.

$H^{13}CO^+$ 1–0 is marginally detected at about 2.5 σ level. With the conversion factor of $S/T_{mb} = 5$ Jy K^{-1}, the velocity-integrated intensity of $H^{13}CO^+$ 1–0 in our result is higher than that of Lindberg et al. (2016) observed with the IRAM PdBI. One possibility of lower $H^{13}CO^+$ emission in Lindberg et al. (2016) might be that $H^{13}CO^+$ emission is extended to more than the beam size of IRAM PdBI, which is similar to SiO 2–1, with higher velocity-integrated intensity in our observation than that with the IRAM PdBI (Lindberg et al. 2016).

NGC 6240: based on the detections of HCN 1–0 and $H^{13}CN$ 3–2 in NGC 6240, $H^{13}CN$ 10 is expected to be detected. However, if the emission around 86340 MHz is identified as $H^{13}CN$ 1–0, even though it is still within the velocity range of HCN 1–0, the central velocity of $H^{13}CN$ 1–0 would deviate from that of HCN 1–0 by approximately +200 km s^{-1}. On the other hand, its central velocity would be consistent with that of HCN 1–0 if it is identified as CH_3OCHO 7–6 (see panels c and d in Fig. 5). Since CH_3OCHO is a complex molecule with low expected abundance, we suggest the emission feature around 86340 MHz is more likely to be $H^{13}CN$ 1–0 than CH_3OCHO 7–6. High sensitivity and high spatial resolution observations are needed to distinguish those possibilities.

For $H^{13}CO^+$ 1–0, if detected, it would be at least partially blended with the SiO 2–1 line, which is shown in panel (e) of Fig. 5. Wang et al. (2013) reported that two features of SiO 2–1 are found in NGC 6240 at $\sim$ 7037 and 7397 km s^{-1}, respectively. As shown in panel (f) of Fig. 5, both SiO 2–1 and $H^{13}CO^+$ 1–0 can contribute the emission feature at $\sim$ 7397 km s^{-1}.

Table 6. Line ratios for HCN, HCO^+, and HNC.

Galaxy	HCN/HNC 1–0	HCN/HCO^+ 1–0
M 82	2.1 ± 0.001	0.66 ± 0.003
NGC 3079	2.6 ± 0.25	0.95 ± 0.15
NGC 4418	2.5 ± 0.25	1.7 ± 0.21
NGC 6240	4.5 ± 0.31	–
NGC 3504	–	–
IC 694	2.2 ± 0.16	0.63 ± 0.01
Mrk 231	2.3 ± 0.12	1.3 ± 0.07
NGC 6946	–	–

4.2 Optical depths in different galaxies

As shown in Tables 3 and 4, based on the HCN/$H^{13}CN$ line ratio, if we assume the $^{12}C/^{13}C$ abundance ratio as 40, the optical depths of HCN 1–0 in M 82, NGC 3079, and NGC 6240 and HNC 1–0 in M 82 and NGC 3079 are obviously optically thin, while they are optically thick in NGC 4418 and Mrk 231. Wang et al. (2016) reported that the optical depth of HCN 1–0 is 6.2 in Arp 220 with assumption of $^{12}C/^{13}C = 40$, which is consistent with our result for the ULIRG galaxies.

On the other hand, with the assumption of $^{14}N/^{15}N = 100$, we obtain a higher optical depths of HCN 1–0 and HNC 1–0 according to HCN/$HC^{15}N$ line ratio than the results with $^{12}C/^{13}C = 40$ in these galaxies. Adopting different abundance ratios, the optical depths of HCN 1–0 and 3–2 in NGC 4418 are always the highest among the eight galaxies with $H^{13}CN$ 1–0 and 3–2 detection, while they are the lowest in M 82. More sources are needed to determine the relationship between the star formation rate and optical depths of dense gas tracers, even though it seems there is already a trend that optical depths are higher in galaxies with more active star formation.

The optical depths of HCN 1–0 and 3–2, HNC and HCO^+ 1–0 also show a large variation, with different abundance ratios of $^{12}C/^{13}C$ and $^{14}N/^{15}N$. It indicates that there are large uncertainties in estimating the dense molecular gas mass only with the measured luminosity of dense gas tracers. For the galaxies without detection of rare isotopologues, we speculate that the optical depth of HCN, HCO^+, and HNC may be low to moderate. As summarized in Table 3, based on the similar beam sizes of HCN 1–0 and 3–2 with those of the IRAM 30-m telescope and the SMT 10-m telescope, we find that the optical depth of HCN 3–2 is higher than that of HCN 1–0 in M 82, NGC 3079, NGC 4418, and NGC 6240, which implies that ground state transitions of dense gas tracers might better trace the star forming gas than high J transitions.

4.3 Line ratios of different dense gas tracers and their isotopologues

4.3.1 Line ratios: dense gas tracers

Line ratios between the ground rotational transitions ($J = 1$–0) of HCN, HNC, and HCO^+ for all detected galaxies are presented in Table 6 . The results of NGC 3079, NGC 4418, Mrk 231, and NGC 6240 are consistent with those observed in Costagliola et al. (2011) and Li et al. (2019). The result for M 82 is consistent with Krips et al. (2008). However, the I(HCN)/I(HNC) 1–0 line ratio of 2.2 in IC 694 is approximately two times larger than the value in Aalto et al. (2002). Our results are more reliable than those in Aalto et al. (2002), as their data were from different observations: HCN 1–0 from Solomon, Downes & Radford (1992) with IRAM

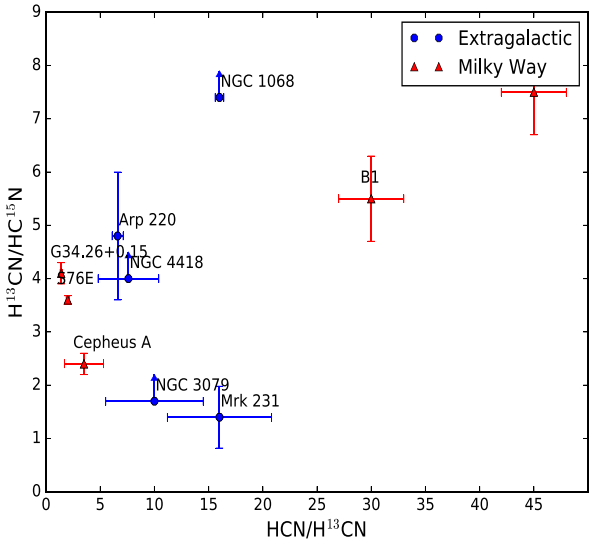

Figure 7. I(H13CN)/I(HC^{15}N) versus I(HCN)/I(H^{13}CN), with the ratios of H13CN/HC^{15}N being on a logarithmic scale. The data of the Milky Way are for massive star-forming regions (Li et al. 2017) and pre-stellar cores (Magalhães et al. 2018).

30-m telescope and HNC from their own observations with 20-m telescope of the Onsala Space Observatory (OSO). However, HCN and HNC 1–0 were obtained simultaneously in our observations, without uncertainties caused by pointing error and absolute flux calibration between different observations.

4.3.2 Isotopic line ratios

The low intensity ratio of H^{13}CN/HC^{15}N may indicate abnormal abundance ratios in both NGC 3079 and Mrk 231 (see Fig. 7). Since H^{13}CN and HC^{15}N are both optically thin and have similar critical densities, the line ratio is directly linked to the abundance ratio of H^{13}CN/HC^{15}N, which is 1.7 in NGC 3079 and 1.4 in Mrk 231. The value is lower than 4.8 found in Arp 220 (Wang et al. 2016) and 11.6 found in NGC 1068 (Wang et al. 2014). Meanwhile, it is within the range of 1.62–4 found in massive star-forming regions and 2–7.5 in pre-stellar cores, respectively (Li et al. 2017; Magalhães et al. 2018, see Fig. 7). To summarize, the measured ratios of H^{13}CN/HC^{15}N show large variations in these galaxies. Moreover, the starburst galaxies show a relatively lower value than those of other galaxies, in agreement with the view of strong ^{15}N enrichment by massive star ejecta in starbursts (Chin et al. 1999).

4.3.3 Isotopic abundance ratios

^{14}N/^{15}N ratios in NGC 3079 and Mrk 231 are derived with the double-isotope method (Adande & Ziurys 2012) with assumption of ^{12}C/^{13}C in previous references: 40 for NGC 3079 (Henkel et al. 1998) and 100 for Mrk 231 (Henkel et al. 2014), respectively. We obtained a ^{14}N/^{15}N abundance ratio of 120 in NGC 3079, which is lower than the value (200–450) in NGC 4945 (Henkel et al. 2018). This ratio is 140 in Mrk 231, which is far lower than the value of ∼400 measured in the nearest ULIRG Arp 220 (Wang et al. 2016). For reference, this ratio in the local interstellar medium is 290 (Adande & Ziurys 2012) and 270 in our Solar system (Dahmen et al. 1995). Although the ^{12}C/^{13}C ratio derived from different tracers may change, it should not change much. We would like to suggest that the uncertainty of ^{12}C/^{13}C ratio is not important for deriving ^{14}N/^{15}N ratio in NGC 3079 and Mrk 231.

Carbon and nitrogen isotopes are thought to be mainly produced from the CNO cycle, their origin still remain uncertain. Milam et al. (2005) and Romano et al. (2017) reported that both chemical fractionation and isotope-selective photodissociation do not play substantial roles in influencing the abundance ratios of ^{12}C/^{13}C and ^{14}N/^{15}N, although the values of the isotopic abundance ratios are affected by high UV radiation and low temperatures. The difference in primary and secondary origins of ^{14}N and ^{15}N may lead to the different ratios of ^{14}N/^{15}N in the galaxies (Romano et al. 2017), which might provide an explanation of the observed low ratios in NGC 3079 and Mrk 231.

5 SUMMARY AND FUTURE PROSPECTS

We carried out single-dish observations towards a sample of eight IR bright galaxies with the SMT 10-m telescope in the 1-mm band and the IRAM 30-m telescope in the 3-mm band to probe the excitation properties of dense gas in these galaxies. We extended the data set for isotopic lines, along with the other effects, which can be used to better estimate dense gas mass and study star formation in galaxies. We obtained the following results:

(1) The isotopic lines of H^{13}CN 3–2 detected in M 82, NGC 3079, NGC 4418, and NGC 6240, and the upper limits in NGC 3504 and NGC 6946 are presented. H^{13}CN 1–0 lines towards M 82, NGC 3079, and Mrk 231 are also detected, while the upper limits of H^{13}CN 1–0 in NGC 6240 and IC 694 are obtained. We also obtain other isotopic lines of dense gas tracers in the 3-mm band: H^{13}CO$^+$ and HN^{13}C 1–0 in M 82, H^{13}CO$^+$, and HC^{15}N 1–0 in NGC 3079, and HC^{15}N 1–0 in Mrk 231.

(2) For M 82, different line profiles of H^{13}CN 1–0 and 3–2 are found. H^{13}CN 1–0 was dominated by the redshifted component of HCN 1–0, while H^{13}CN 3–2 was dominated by the blueshifted component of HCN 3–2. Different line profiles of H^{13}CN 3–2 and 1–0 are also found in NGC 3079, which indicates that the blue velocity component of the molecular gas may be warmer and denser than the red velocity component.

(3) Based on the large variations in optical depths of HCN 1–0 and 3–2 in different types of galaxies, our results suggest that large uncertainties in estimating dense gas masses using only the line luminosity of dense gas tracers, such as HCN 1–0, 3–2, etc.

(4) The optical depths of HCN 1–0 are lower than that of HCN $J = 3$–2 in M 82, NGC 3079, NGC 4418, and NGC 6240, which implies that the HCN $J = 3$–2 line is more easily saturated than the transition of $J = 1$–0. We suggest that ground state transitions of dense gas tracers might be better for tracing star-forming gas than the high transition ones.

(5) Based on the low line ratio of H^{13}CN/HC^{15}N 1–0, the low ^{14}N/^{15}N ratios in NGC 3079 and Mrk 231 are found to be 120 and 140, respectively, which are much lower than those for the local interstellar medium.

Our observations reported here suggest that observing the rare isotopologues of dense gas tracers toward galaxies near and far with ALMA, can be a powerful tool to exactly determine physical conditions of the very dense star forming molecular gas in galaxies.

ACKNOWLEDGEMENTS

We are grateful to the staff of the SMT 10-m telescope and IRAM 30-m telescope for their kind help and support during our observa-

tions. This work is supported by the National Key R&D Program of China (no. 2017YFA0402704), the Natural Science Foundation of China under grants of 11590783 and Natural Science Foundation of Hebei Province (A2019205100). This work also benefitted from the International Space Science Institute (ISSI/ISSI-BJ) in Bern and Beijing, thanks to the funding of the team 'Chemical abundances in the ISM: the litmus test of stellar IMF variations in galaxies across cosmic time' (PI: DR and Z-YZ). YG's research is supported by National Key Basic Research and Development Program of China (grant No. 2017YFA0402704), National Natural Science Foundation of China (grant Nos. 11861131007, U1731237 and 11420101002), and Chinese Academy of Sciences Key Research Program of Frontier Sciences (grant No. QYZDJSSW-SLH008). This research has made use of the NASA/IPAC Extragalactic Database (NED), which is operated by the Jet Propulsion Laboratory, California Institute of Technology, under contract with the National Aeronautics and Space Administration.

REFERENCES

Aalto S., Monje R., Martín S., 2007, A&A, 475, 479
Aalto S., Polatidis A. G., Hüttemeister S., Curran S. J., 2002, A&A, 381, 783
Adande G. R., Ziurys L. M., 2012, ApJ, 744, 194
Aladro R. et al., 2015, A&A, 579, A101
Chin Y.-n., Henkel C., Langer N., Mauersberger R., 1999, ApJ, 512, L143
Clayton D. D., Nittler L. R., 2004, ARA&A, 42, 39
Costagliola F. et al., 2011, A&A, 528, A30
Costagliola F. et al., 2015, A&A, 582, A91
Dahmen G., Wilson T. L., Matteucci F., 1995, A&A, 295, 194
Elmegreen D. M., Chromey F. R., Santos M., Marshall D., 1997, AJ, 114, 1850
Feruglio C., Fiore F., Piconcelli E., Cicone C., Maiolino R., Davies R., Sturm E., 2013, A&A, 558, A87
Fuente A. et al., 2008, A&A, 492, 675
Gallagher M. J. et al., 2018, ApJ, 868, L38
Gao Y., Solomon P. M., 2004a, ApJS, 152, 63
Gao Y., Solomon P. M., 2004b, ApJ, 606, 271
García-Burillo S., Martín-Pintado J., Fuente A., Usero A., Neri R., 2002, ApJ, 575, L55
Goldsmith P. F., Langer W. D., 1999, ApJ, 517, 209
Greve T. R., Papadopoulos P. P., Gao Y., Radford S. J. E., 2009, ApJ, 692, 1432
Henkel C., Chin Y.-N., Mauersberger R., Whiteoak J. B., 1998, A&A, 329, 443
Henkel C. et al., 2014, A&A, 565, A3
Henkel C. et al., 2018, A&A, 615, A155
Izumi T. et al., 2013, PASJ, 65, 100
Jiang X., Wang J., Gu Q., 2011, MNRAS, 418, 1753
Kennicutt R. C., Evans N. J., 2012, ARA&A, 50, 531
Kepley A. A., Leroy A. K., Frayer D., Usero A., Marvil J., Walter F., 2014, ApJ, 780, L13
Koda J., Sofue Y., Kohno K., Nakanishi H., Onodera S., Okumura S. K., Irwin J. A., 2002, ApJ, 573, 105
Kohno K., 2005, in Hüttmeister S., Manthey E., Bomans D., Weis K., eds, AIP Conf. Ser. Vol. 783, The Evolution of Starbursts, p. 203
Kohno K., Kawabe R., Vila-Vilaró B., 1999, ApJ, 511, 157
Krips M., Neri R., García-Burillo S., Martín S., Combes F., Graciá-Carpio J., Eckart A., 2008, ApJ, 677, 262
Lada E. A., 1992, ApJ, 393, L25
Li F., Wang J., Kong M., Li S., 2019, MNRAS, 482, 4763
Li F. et al., 2020, PASJ, in press
Lindberg J. E. et al., 2016, A&A, 587, A15
Li S. et al., 2017, MNRAS, 466, 248
Magalhães V. S., Hily-Blant P., Faure A., Hernandez-Vera M., Lique F., 2018, A&A, 615, A52
Manohar S., Scoville N., 2017, ApJ, 835, 127
Martín S., Aladro R., Martín-Pintado J., Mauersberger R., 2010, A&A, 522, A62
Mauersberger R., Henkel C., 1989, A&A, 223, 79
Milam S. N., Savage C., Brewster M. A., Ziurys L. M., Wyckoff S., 2005, ApJ, 634, 1126
Mo H., van den Bosch F. C., White S., 2010, Galaxy Formation and Evolution
Müller H. S. P., Schlöder F., Stutzki J., Winnewisser G., 2005, J. Mol. Struct., 742, 215
Narayanan D., Krumholz M. R., Ostriker E. C., Hernquist L., 2012, MNRAS, 421, 3127
Nguyen Q.-R., Jackson J. M., Henkel C., Truong B., Mauersberger R., 1992, ApJ, 399, 521
Paglione T. A. D., Jackson J. M., Ishizuki S., 1997, ApJ, 484, 656
Pan H.-A., Kuno N., Koda J., Hirota A., Sorai K., Kaneko H., 2015, ApJ, 815, 59
Papadopoulos P. P., 2007, ApJ, 656, 792
Papadopoulos P. P. et al., 2014, ApJ, 788, 153
Pickett H. M., Poynter R. L., Cohen E. A., Delitsky M. L., Pearson J. C., Müller H. S. P., 1998, J. Quant. Spec. Radiat. Transf., 60, 883
Pérez-Beaupuits J. P., Aalto S., Gerebro H., 2007, A&A, 476, 177
Romano D., Matteucci F., Zhang Z.-Y., Papadopoulos P. P., Ivison R. J., 2017, MNRAS, 470, 401
Saito T. et al., 2018, ApJ, 863, 129
Sakai S., Madore B. F., 1999, ApJ, 526, 599
Sanders D. B., Mazzarella J. M., Kim D.-C., Surace J. A., Soifer B. T., 2003, AJ, 126, 1607
Shimajiri Y. et al., 2017, A&A, 604, A74
Solomon P. M., Downes D., Radford S. J. E., 1992, ApJ, 387, L55
Spilker J. S. et al., 2014, ApJ, 785, 149
Spoon H. W. W., Keane J. V., Tielens A. G. G. M., Lutz D., Moorwood A. F. M., 2001, A&A, 365, L353
Tang X. D. et al., 2019, A&A, 629, A6
Tan Q.-H. et al., 2018, ApJ, 860, 165
Tsai M., Hwang C.-Y., 2015, AJ, 150, 43
Tunnard R., Greve T. R., Garcia-Burillo S., Graciá Carpio J., Fuente A., Tacconi L., Neri R., Usero A., 2015, ApJ, 815, 114
Wang J., Zhang J., Shi Y., Zhang Z., 2013, ApJ, 778, L39
Wang J., Zhang Z.-Y., Qiu J., Shi Y., Zhang J., Fang M., 2014, ApJ, 796, 57
Wang J., Zhang Z.-Y., Zhang J., Shi Y., Fang M., 2016, MNRAS, 455, 3986
Watanabe Y., Sakai N., Sorai K., Yamamoto S., 2014, ApJ, 788, 4
Wu J., Evans N. J., II, Gao Y., Solomon P. M., Shirley Y. L., Vanden Bout P. A., 2005, ApJ, 635, L173
Zhang J. S., Henkel C., Guo Q., Wang J., 2012, A&A, 538, A152
Zhang Z.-Y., Gao Y., Henkel C., Zhao Y., Wang J., Menten K. M., Güsten R., 2014, ApJ, 784, L31

APPENDIX A: A SUMMARY OF OBSERVING PARAMETERS

Table A1. The basic properties of the sample galaxies with the SMT 10-m telescope.

Source	Line	On-source time (min)	T_{sys} (K)	Resolution (pc)
M 82	HCN(3–2)	6	235	529.4
	$H^{13}CN$(3–2)	174	194	548.3
NGC 3079	HCN(1–0)	6	229	2185.5
	$H^{13}CN$(3–2)	123	199	2263.6
NGC 3504	HCN(3–2)	9	224	1099.6
	$H^{13}CN$(3–2)	174	174	1138.8
NGC 4418	HCN(3–2)	6	229	3936.7
	$H^{13}CN$(3–2)	105	235	4077.3
NGC 6240	HCN(3–2)	6	234	13303.4
	$H^{13}CN$(3–2)	101	197	13778.4
NGC 6946	HCN(3–2)	18	357	746.6
	$H^{13}CN$(3–2)	54	206	773.3

Table A2. The basic properties of the sample galaxies with the IRAM 30-m telescope.

Source	Line	Dates of observations[a]	On-source time (min)	T_{sys} (K)	LO[b] (GHz)	Resolution (pc)
M 82	$H^{13}CN$(1–0)	2017-06-27	63	85	95.8	548.3
		2017-06-30	43	94	94.9	
NGC 3079	$H^{13}CN$(1–0)	2017-06-27	37	90	95.8	2263.6
		2017-06-28	54	92	95.3	
		2017-07-01	31	93	95.0	
IC 694	$H^{13}CN$(1–0)	2017-06-28	37	97	95.3	6706.4
		2017-06-30	44	91	94.9	
Mrk 231	$H^{13}CN$(1–0)	2017-07-01	45	94	95.0	24604.3
		2017-07-02	108	89	94.5	
NGC 6240	$H^{13}CN$(1–0)	2017-06-27	54	85	95.8	13778.4
		2017-06-28	30	92	95.3	
		2017-06-30	35	89	94.9	
		2017-07-01	51	92	95.0	
		2017-07-02	24	87	95.1	

Notes: [a]The date of the observations is listed in format of YYYY-MM-DD.
[b]LO is the local oscillator tuning setups during the observations.

APPENDIX B: DETECTED LINES IN EACH GALAXY

Table B1. Results for M 82.

Line	Frequency (GHz)	I (K km s^{-1})	V_{LSR} (km s^{-1})	Line width (km s^{-1})
$H^{13}CN$ 1–0	86.340	0.22 ± 0.03	–	171
		0.32 ± 0.03	–	144
$H^{13}CO^+$ 1–0	86.754	0.3 ± 0.04	133 ± 11	99 ± 22
		0.32 ± 0.05	295 ± 7.9	108 ± 21
$HN^{13}C$ 1–0	87.091	0.17 ± 0.03	272 ± 18	172 ± 33
HCN 1–0	88.632	14.7 ± 0.06	155 ± 0.04	124 ± 0.5
		12.9 ± 0.05	292 ± 0.2	104 ± 0.4
HCO^+	89.189	24.8 ± 0.08	163 ± 0.2	132 ± 0.5
		16.7 ± 0.07	299 ± 0.17	100 ± 0.35
HNC 1–0	90.663	7.1 ± 0.06	146 ± 0.56	121 ± 1.2
		6.3 ± 0.06	291 ± 0.49	105 ± 0.99
$H^{13}CN$ 3–2	259.012	0.2 ± 0.04	138 ± 23	185.7 ± 48.5
HCN 3–2	265.886	2.6 ± 0.35	136 ± 7	116 ± 16
		4.2 ± 0.35	284 ± 4	113 ± 10

Notes: $HC^{15}N$ and $H^{15}NC$ 1–0 are blended by SO and CH_3OCHO, respectively. Although we treat the $HC^{15}N$ 1–0 and $H^{15}NC$ 1–0 as non-detections, the high velocity components of the emission at approximately 86055 MHz might be $HC^{15}N$ 1–0 and the low velocity components of another emission at approximately 88865 MHz might be $H^{15}NC$ 1–0. For $H^{13}CN$ 1–0, the velocity range is used to estimate the line intensities, instead of the results from Gaussian fitting.

Table B2. Results for NGC 3079.

Line	Frequency (GHz)	I (K km s^{-1})	$V_{\rm LSR}$ (km s^{-1})	Line width (km s^{-1})
$H^{13}CN$ 1–0	86.340	0.3 ± 0.05	1278 ± 11	122 ± 23
$HC^{15}N$ 1–0	86.055	<0.08(3σ)	–	136
		0.1 ± 0.03	1287 ± 25	136 ± 36
$H^{13}CO^+$ 1–0	86.754	0.4 ± 0.07	1285 ± 22	216 ± 51
SiO 2–1	86.847	0.2 ± 0.05	1238 ± 19	129 ± 37
$HN^{13}C$ 1–0	87.091	<0.08(3σ)	–	224
HCN 1–0	88.632	2.6 ± 0.1	999 ± 4.6	238 ± 9
		3 ± 0.1	1285 ± 3.6	224 ± 7
$H^{15}NC$ 1–0	88.866	< 0.1 (3σ)	–	224
HCO^+ 1–0	89.188	3.1 ± 0.4	1004 ± 15	269 ± 28
		2.8 ± 0.4	1300 ± 14	236 ± 26
HNC 1–0	90.664	0.8 ± 0.1	971 ± 13	220 ± 27
		1.4 ± 0.1	1265 ± 9	245 ± 18
$H^{13}CN$ 3–2	259.012	0.1 ± 0.03	1034 ± 11	55.1 ± 25.3
HCN 3–2	265.886	0.5 ± 0.1	1035 ± 7	55.3 ± 14.9
		1.0 ± 0.2	1189 ± 21	178.1 ± 49.0

Notes: We use the redshift component line width to estimate the upper integrated intensity limit the blueshift component of $HC^{15}N$. We estimate the upper limit of $HN^{13}C$ and $H^{15}NC$ integrated intensities with the redshift component line width of HCN 1–0.

Table B3. Results for NGC 3504 and NGC 6946.

Galaxy	Molecular	Flux (K km s^{-1})	Velocity (km s^{-1})	Line width (km s^{-1})
NGC 3504	HCN 3–2	0.9 ± 0.2	1538 ± 10	119.3 ± 22.7
	$H^{13}CN$ 3–2	<0.07(3σ)	–	119
NGC 6946	HCN 3–2	1.5 ± 0.3	77 ± 9	107.9 ± 37.2
	$H^{13}CN$ 3–2	<0.08(3σ)	–	107.9

Notes: NGC 3504 and NGC 6946 are just observed with the SMT 10-m telescope in the 1-mm band. We estimate the upper limit of $H^{13}CN$ 3–2 integrated intensity with the line width of HCN 3–2.

Table B4. Results for IC 694.

Line	Frequency (GHz)	I (K km s^{-1})	$V_{\rm LSR}$ (km s^{-1})	Line width (km s^{-1})
$H^{13}CN$ 1–0	86.340	<0.2(3σ)	–	288[a]
$HC^{15}N$ 1–0	86.055	<0.2(3σ)	–	288[a]
$H^{13}CO^+$ 1–0	86.754	<0.2(3σ)	–	275[a]
SiO 2–1	86.847	<0.1(3σ)	–	288[a]
$HN^{13}C$ 1–0	87.091	<0.14(3σ)	–	271[a]
HCN 1–0	88.632	2.2 ± 0.04	3037 ± 2.5	288 ± 5
HCO^+ 1–0	89.188	3.5 ± 0.05	3065 ± 2.2	275 ± 5
HNC 1–0	90.663	1.0 ± 0.07	3085 ± 9.5	271 ± 18
$H^{15}NC$ 1–0	88.866	<0.23(3σ)	–	271

Notes: We use the line width of HCN 1–0 to estimate the upper integrated intensity limit of $H^{13}CN$, $HC^{15}N$, $H^{13}CO^+$, and SiO. For $HN^{13}C$ and $H^{15}NC$, the upper limits are estimated using the the line width of HNC 1–0. [a] is the line width, which is used to calculated the upper limits of the undetected lines.

Table B5. Results for NGC 4418.

Line	Frequency (GHz)	I (K km s^{-1})	$V_{\rm LSR}$ (km s^{-1})	Line width (km s^{-1})	Reference
$H^{13}CN$ 1–0	86.340	0.33 ± 0.12	–	150 ± 33	3
$HC^{15}N$ 1–0	86.055	<0.003(3σ)	–	140 ± 10[a]	2
$H^{13}CO^+$ 1–0	86.754	<0.38(3σ)	–	–	3
HCN 1–0	88.632	2.5 ± 0.18	–	188 ± 33	3
$H^{15}NC$ 1–0	88.866	<0.0025(3σ)	–	110 ± 10[a]	2
HCO^+ 1–0	89.188	1.5 ± 0.15	–	133 ± 33	3
HNC 1–0	90.663	1.0 ± 0.07	–	150 ± 18	3
$H^{13}CN$ 3–2	259.012	0.36 ± 0.05	2100 ± 15	196 ± 30	1
HCN 3–2	265.886	1.1 ± 0.26	2065 ± 22	165 ± 40	1

Notes: For $HC^{15}N$ 1–0 and $H^{15}NC$ 1–0, we used the noise level of $H^{13}CN$ 1–0 and the width of HCN 1–0 and HNC 1–0 in Costagliola et al. (2015) to estimate their upper 3σ limit. The velocity-integrated intensities are in $T_{\rm mb}$ instead of T_A^*. The references 1: this work, 2: Costagliola et al. (2015), and 3: Costagliola et al. (2011).
[a] is the line width, which is used to calculated the upper limits of the undetected lines.

Table B6. Results for Mrk 231.

Line	Frequency (GHz)	I (K km s^{-1})	$V_{\rm LSR}$ (km s^{-1})	Line width (km s^{-1})
$H^{13}CN$ 1–0	86.340	0.1 ± 0.03	12143 ± 17	152 ± 37
$HC^{15}N$ 1–0	86.055	0.07 ± 0.02	12158 ± 20	107 ± 31
$H^{13}CO^+$ 1–0	86.754	0.1 ± 0.04	12098 ± 47	190 ± 94
SiO 2–1	86.847	0.14 ± 0.03	12129 ± 8	83 ± 15
$HN^{13}C$ 1–0	87.091	<0.1(3σ)	–	183
HCN 1–0	88.632	1.6 ± 0.05	12137 ± 3.1	183 ± 8
HCO^+ 1–0	89.188	1.2 ± 0.05	12142 ± 3.3	185 ± 8
HNC 1–0	90.663	0.7 ± 0.03	12149 ± 4.3	188 ± 11
$H^{15}NC$ 1–0	888.657	< 0.1 (3σ)	–	183

Notes: $H^{13}CO^+$ 1–0 is only tentatively detected with 2.5σ. We estimate the upper limit of $HN^{13}C$ and $H^{15}NC$ 1–0 integrated intensities with the line width of HNC 1–0.

Table B7. Results for NGC 6240.

Line	Frequency (GHz)	I (K km s^{-1})	$V_{\rm LSR}$ (km s^{-1})	Line width (km s^{-1})
$H^{13}CN$ 1–0	86.340	≤0.06(4σ)	–	79 ± 23
$H^{13}CO^+$ 1–0	86.754	< 0.1[a]	–	–
SiO 2–1	86.847	<0.15[a]	–	–
$HN^{13}C$ 1–0	87.091	<0.057 (3σ)	–	310
HCN 1–0	88.632	2.7 ± 0.05	7188 ± 3	375 ± 8
$H^{15}NC$ 1–0	88.866	< 0.08 (3σ)	–	310
HNC 1–0	90.663	0.6 ± 0.04	7183 ± 9	310 ± 26
$H^{13}CN$ 3–2	259.012	0.15 ± 0.05	7125 ± 17	89.8 ± 23.5
HCN 3–2	265.886	1.7 ± 0.3	7227 ± 20	222.0 ± 38.7

Notes: The emission feature around 86 340 MHz is possible to be $H^{13}CN$, due to there is a 4σ level emission feature around 86 340 MHz. The 3σ upper limits of $HN^{13}C$ and $H^{15}NC$ 1–0 intensity are estimated with the line width of HNC 1–0, and $HC^{15}N$ 1–0 is outside the covered frequency range.
[a] Due to $H^{13}CO^+$ 1–0 is possibly blended with SiO 2–1 emission, we could not extract the spectrum of these two species properly. So the upper limit of integrate intensity for them are estimated.

APPENDIX C: SPECTRUM OF ALL FIVE GALAXIES IN THE 3-MM BAND WITH IRAM 30-M TELESCOPE

With the 1-GHz bandwidth of SMT, we obtain only $H^{13}CN$ 3–2 and HCN 3–2 in the centre of the band. Therefore, we do not show the spectra of all sources at 1-mm band. In addition, we show only the spectra of M 82, NGC 3079, NGC 6240, IC 694, and Mrk 231 between 86 and 90 GHz with IRAM 30-m telescope. The *Y*-axis of each spectra is amplified to show these weak isotopic lines in these sources.

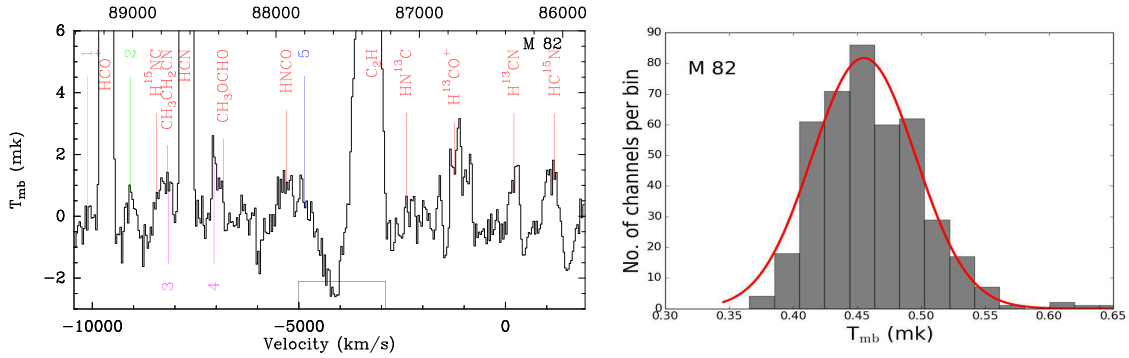

Figure C1. Left: molecular species of M 82 between 86 and 90 GHz. The components 1 and 2 emission features might be from the molecular gas outflow traced by HCO^+ (Kepley et al. 2014); and components 3 and 4 emission features may be from the outflowing gas traced by HCN or from both CH_3CH_2CN and CH_3OCHO emissions. We classify the emission feature at approximately 87 856 MHz as unidentified line for component 5. Due to each band has two 2 sidebands (L,U), which are split in two blocks, denoted by I and O (inner and outer). Therefore, there are two parts (LO and LI) in the LSB. The window is the connection of LO and LI band, which is the range of frequency variation, due to different LO tuning setups are used during the observation. The isotopic lines of dense gas tracers are not located in this window. Right: distribution of the noise between 86 and 90 GHz. The rms is 0.46 mK at a velocity resolution of 36.62 km s^{-1}.

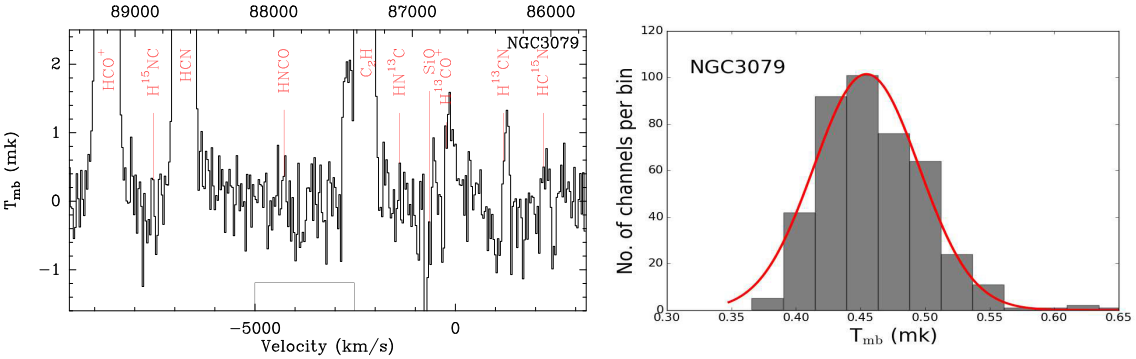

Figure C2. Left: molecular species of NGC 3079 between 86 and 90 GHz. We estimate only the upper integrated intensity limit of $HN^{13}C$ and $H^{15}NC$. See the caption of Fig. C1 for more details of the window in the *X*-axis. Right: distribution of the noise between 86 and 90 GHz. The rms is 0.45 mK at a velocity resolution of 36.6 km s^{-1}.

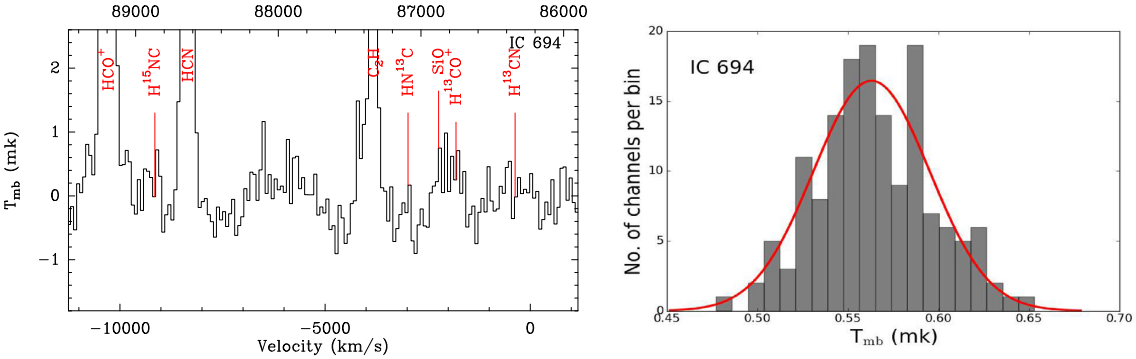

Figure C3. Left: molecular species of IC 694 between 86 and 90 GHz. No isotopic lines of dense gas tracers are detected in IC 694. Upper limits of the integrated intensity for each isotopologues were derived. See the caption of Fig. C1 for more details of the window in the *X*-axis. Right: distribution of the noise between 86 and 90 GHz. The rms is 0.56 mK at a velocity resolution of 37.05 km s^{-1}.

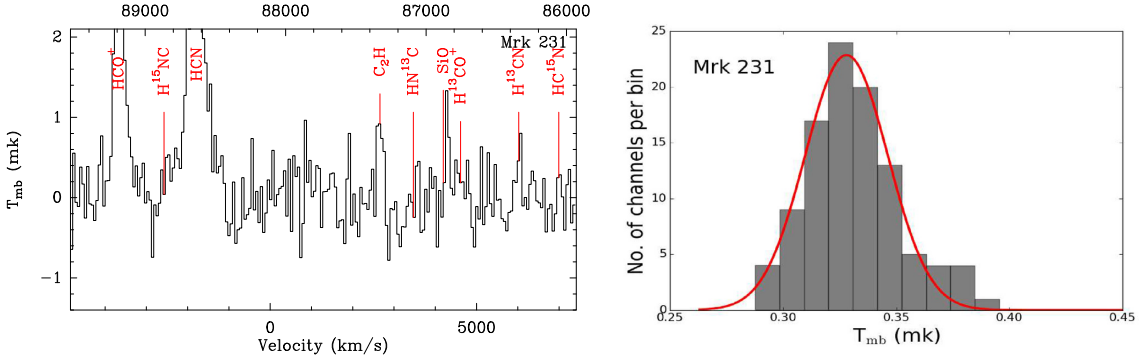

Figure C4. Left: molecular species of Mrk 231 between 86 and 90 GHz. We estimate the upper integrated intensity limit of $HN^{13}C$ and $H^{15}NC$ and $H^{13}CO^+$ 1–0 is only tentatively detected with 2.5σ. Right: distribution of the noise between 86 and 90 GHz. The rms is 0.33 mK at a velocity resolution of 56.1 km s^{-1}.

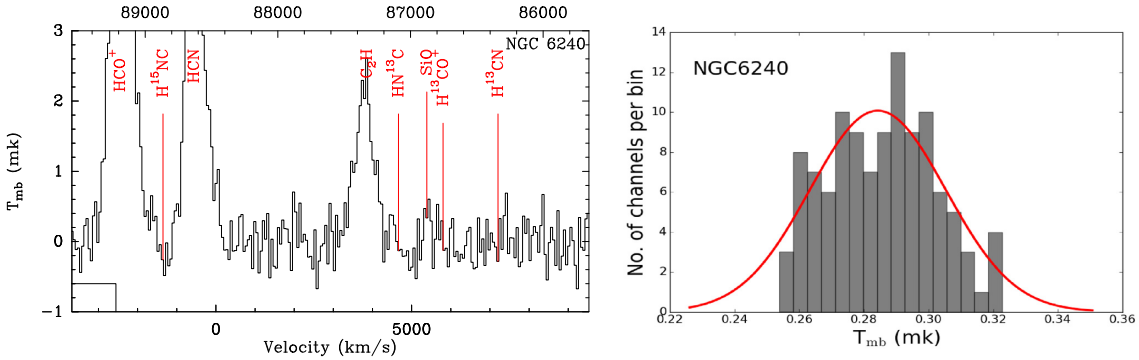

Figure C5. Left: molecular species of NGC 6240 between 86 and 90 GHz. The emission feature around 86 340 MHz is possible to be $H^{13}CN$, due to there is a 4σ level emission feature around 86 340 MHz. Non-detection of the other rare isotopic lines are presented. We estimate the upper integrated intensity limit of $H^{15}NC$. See the caption of Fig. C1 for more details of the window in the *X*-axis. Right: distribution of the noise between 86 and 90 GHz. The rms is 0.28 mK at a velocity resolution of 54.93 km s^{-1}.

APPENDIX D: THE NOISE SPECTRUM OF NGC 3079 IN THE 3-MM BAND WITH IRAM 30-M TELESCOPE

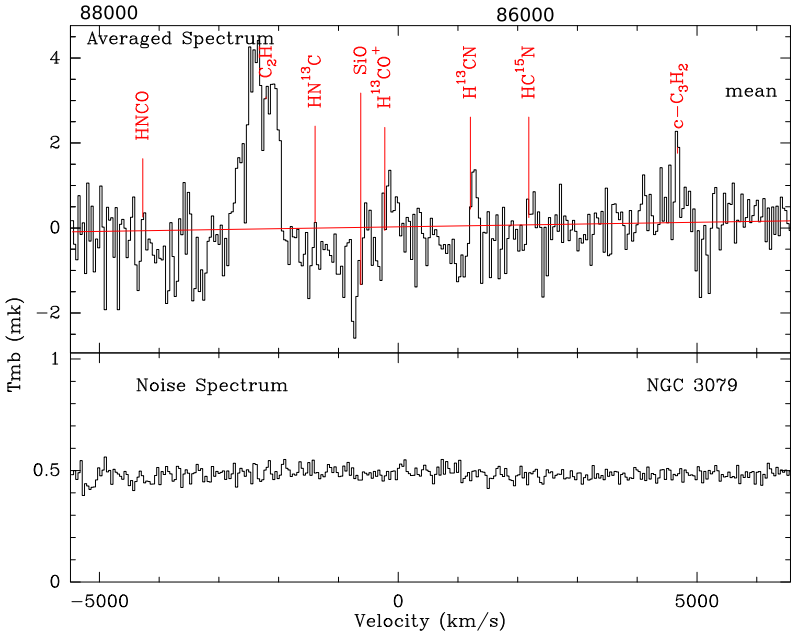

Figure D1. The noise spectrum of NGC 3079. Band ranges from 84 to 88 GHz, with rms of 0.73 mK at the velocity resolution of 36 km s^{-1}s. The red line is 1 rms levels derived from first-order baseline fitting. The upper panel is the average spectrum of NGC 3079 and the lower panel is the noise spectrum.

This paper has been typeset from a TEX/LATEX file prepared by the author.